[**Chapter 4:** Studies of $La_{0.67}Sr_{0.33}Mn_{1-x}Fe_xO_3$(x=0.15, 0.25 and 0.35) prepared by Planetary Ball Milling Method]

4.1 Introduction

Renewed interest in the study on manganite ceramics and their thin films is accelerated in recent time due to their rich physics and potential applications in variety of devices [1-4]. This credit goes to the excellent experimental and theoretical methodologies which have helped in the proper development and understanding of structure property relation. Hole doped perovskite manganites of type $RE_{1-x}A_xMnO_3$ (RE being rare earth ion and A divalent ion such as A=Ca, Sr, Ba and Pb) are being revisited for the study of their magnetoresistance (MR) properties [2-4]. To attain this, many groups have substituted various types of dopants at both A-site (RE) and B-site (Mn) in ABO_3 type $RE_{1-x}A_xMnO_3$ perovskite manganites [5-8]. They depict half metallic behavior or spin polarized conduction and other remarkable features which opened up a new door of fascinating world, named as a mixed valent manganites [9]. The mixed valent manganites contain both Mn^{3+} and Mn^{4+}. There exist reports on the creation of Mn^{4+} even without doping at the A-site due to the defective structure of perovskite [10, 11]. This defective structure of perovskite is mainly distinguished by orthorhombic, rhombohedral and cubic phases [12, 13]. This structural behavior can be used as a prominent way to explain different CMR properties. The rhombohedral phase suppresses the co-operative JT distortion which makes hole induced ferromagnetism [14]. Furthermore, the existing Zener double exchange mechanism (ZDE), electron–phonon coupling (EPC) and most importantly newly discovered phenomena of colossal magnetoresistance (CMR) draw attention towards the manganites [3, 15- 17]. Fig. 4.1 depicts phase diagram of the manganite systems $La_{1-x}Sr_xMnO_3$.

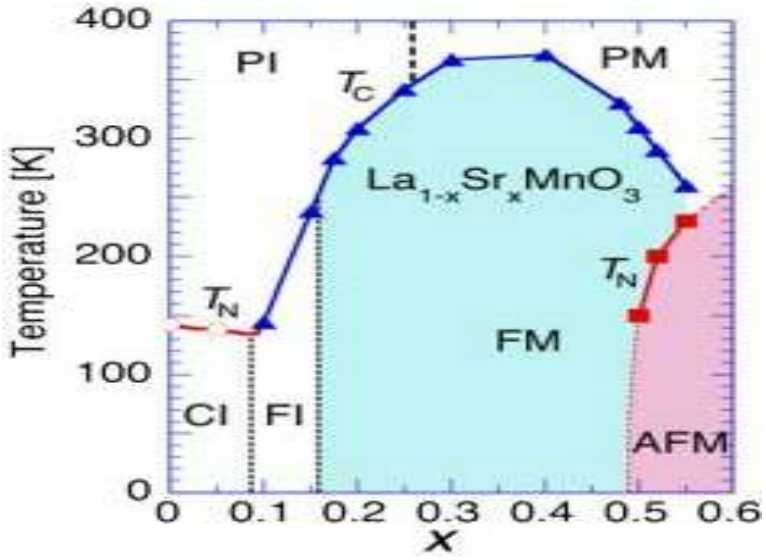

Fig. 4.1: Phase diagram of $La_{1-x}Sr_xMnO_3$ manganite system [18].

These manganite materials exhibit metal to insulator transition as well as ferromagnetic to paramagnetic transition. The rare earth and alkaline earth trivalent and divalent ions respectively occupy the A-site with 12-fold oxygen coordination, while the smaller Mn ion at B site occupies center of an oxygen octahedron with 6-fold coordination. The d-orbital of the manganese ion split into three fold degenerate t_{2g} states while two fold degenerate e_g states are separated by the field energy for BO_6 octahedra. The A and B sites are occupied by La or Sr and Mn respectively as shown in Fig. 4.2.

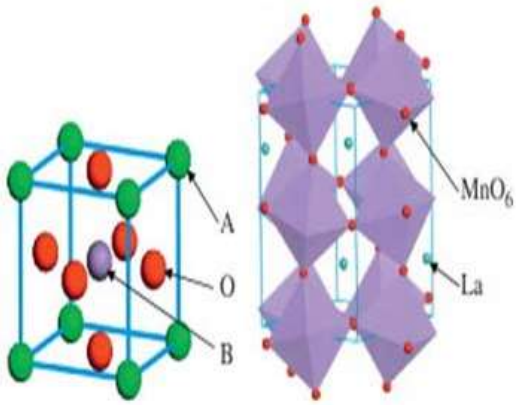

Fig. 4.2: Crystal structure of ABO_3 with MnO_6 octahedral [19].

The bond length and bond angle of Mn^{3+}-O-Mn^{4+} in rhombohedral $La_{1-x}Sr_xMnO_3$ (LSMO) play an imperative role in controlling the CMR properties [20]. The parent compound $LaMnO_3$ (LMO) behaves as an antiferromagnetic insulator, while the hole–doped system shows metal-insulator transition with ferromagnetic (FM) transition [21]. The magnetoresistance effect increases with doping of cation at rare earth and Mn–sites. The above mentioned factor significantly affects physical properties of these CMR materials.

The synthesis of the compounds in the form of nanoscale powders are an important aspect in the field of materials science. Several methods of synthesis and preparation of these materials which can give homogeneous materials are often used as security for the homogenization of materials invested in various fields of industry. These are coprecipitation or precipitation, sol–gel, ball milling and the conventional ceramic methods [22]. The ball milling method has become one of the important methods in general synthesis and in particular powder metallurgy due to high flexibility, controlled process parameters and wide range of productively materials [23]. The stable FM metallic phase persists up to almost half doping level of strontium (Sr). To clarify the mechanism of the CMR effect in $La_{1-x}Sr_xMnO_3$, (LSMO) various elements, suchas Fe, Cr, Ga, Al, Ti, Cu, and Ru [24-26] are substituted for Mn due to the crucial role of Mn ion in CMR. The experiments show that the Mn site doping weakens long-range FM ordering and hence decreases Curie temperature. Furthermore, magnetic and non-magnetic ions doping at Mn-sites results a different effect [24]. It is found that the Mn-site doping mainly focuses on FM metallic compounds LSMO. However, the substitution of Fe^{3+} ions in manganites deserves a particular attention as there exist few disputes in the case of double exchange mechanism as far as influence of Fe^{3+} ions is concerned [23, 27]. The Fe^{3+} ions built into the Mn^{3+}–O^{2-}–Mn^{4+} chains [28]. The Fe^{3+} doping at Mn sites result in high MR values with a low

magnitude of the applied magnetic field. We propose to conduct a systematic investigation to understand the mechanism of structural, morphological, electronic, magnetic and vibrational properties that evolve with changes in Fe^{3+} concentrations at the Mn site [28]. The substitution of Fe ions at Mn site is of particular interest due to the fact that the Fe ions replace Mn ions without any structural deformation due to their similar ionic radii [29].

This chapter presents the step wise synthesis procedure of Fe doped LSMO (LSMFO) compounds and analysis of the results obtained after employing the various techniques for phase analysis, chemical composition study, elemental analysis, structural and morphological study, vibrational properties and magnetic properties. The analysis of results is also done using *state-of-the-art* density functional theory (DFT) based ab-initio calculations. The calculated formation energy, structural, electronic and vibrational properties are discussed in light of synthesized LSMFO samples.

4.2 Synthesis and Experimental Details

A series of polycrystalline samples of $La_{0.67}Sr_{0.33}Mn_{1-x}Fe_xO_3$ (x=0.15, 0.25, 0.35) were synthesized by the solid state reaction route using standard planetary ball milling method. Stoichiometric mixtures of oxides precursors in the dried forms of La_2O_3, SrO, MnO_2, and Fe_2O_3 (All AR Grade) up to 99% purity in the appropriate proportions according to the following reaction is used:

$$0.335La_2O_3 + 0.33SrO + (1-x)MnO_2 + \frac{x}{2}Fe_2O_3 \rightarrow 0.67La_2O_3 + 0.33SrO + Mn(1-x)Fe_xO_3 \quad (1)$$

In order to reduce the particle size of LSMFO sample, the powder has been subjected to the mechanical milling process in air atmosphere by using a planetary ball milling Fritsh PULVERISETTE 5 [1, 23]. For this, the rotation speed and ball to powder ratio were chosen to be around 250 to 350 rpm and 10:1 respectively. The mixture of manganite powders has been

milled for approximately 7 hours. The obtained powder was then grinded in agate mortar and pestle for the calcination procedure. The powders were calcined at 800ºC, 900ºC, 1000ºC and 1100ºC for 7 to 8 hours in a box furnace and cooled naturally to room temperature. The pictorial presentation of the formation of samples is shown in Fig. 4.3.

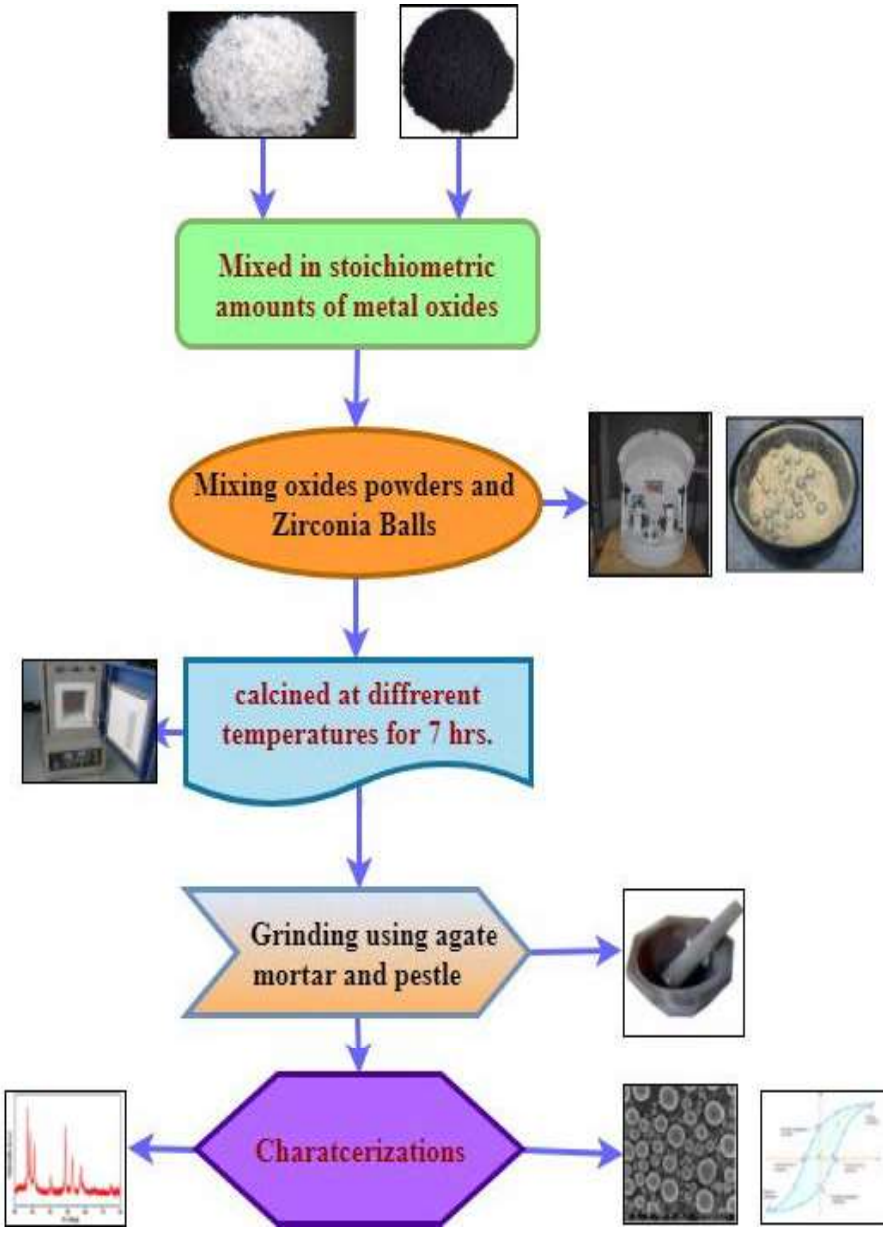

Fig. 4.3: Synthesis chart of Fe doped LSMO using ball milling method.

Phase purity crystal properties and homogeneity of samples of prepared samples were performed by powder X-ray diffraction (XRD) at room temperature using a PANalytical X'Pert Pro with Cu-Kα radiation (λ=1.5406 Å). The X-ray diffraction patterns were fitted by Rietveld refinement using FullProf program in order to obtain structural parameters for each sample having different doping concentration at different temperature. Similarly, magnetic properties were acquired from magnetization versus temperature and applied magnetic field plot recorded by PPMS SQUID magnetometer. The magnetization versus applied magnetic field study up to 100 Oe for few samples was performed at low temperature (3K) and room temperature (300K) for both zero field cooled and field cooled. The surface morphology, grain size and elemental analysis of the synthesized polycrystalline samples were evaluated by an analytical field emission scanning electron microscope (FE-SEM) using JEOL JSM-7600F and Oxford INCA Energy Dispersive Analysis of X-ray (EDAX). The vibrational properties were recorded by Raman spectroscopy using JOBIN YVON HORIBA-HR800 at room as well as low temperature (80K) with back scattering geometry of the incident laser light. The samples were excited with 632.8 nm line of HeNe ion laser with the liquid nitrogen cooled charged couple device (CCD) detector.

4.3 Results and Discussion

4.3.1 X-Ray Diffraction

To verify the crystal structure, phase formation and lattice parameters, X-ray diffraction patterns (XRD) were obtained at room temperature. X-ray diffraction pattern of $La_{0.67}Sr_{0.33}Mn_{1-x}Fe_xO_3$ series with (x=0.15, 0.25, 0.35) at various calcined temperatures (T= 800ºC to 1100ºC) of polycrystalline samples are simultaneously depicted in Fig. 4.4. The measurement parameters were scanned over $20^o \leq 2\theta \leq 80^o$ with step size of 0.02. Powder X-ray diffraction studies

showed that the LSMFO samples are single phase with no detectable impurity peaks within XRD limit and the samples exist in distorted perovskite structure. This means that the perovskite phase of Fe doped LSMO is obtained from the precursors without any significant segregation of the individuals metals [1, 23].

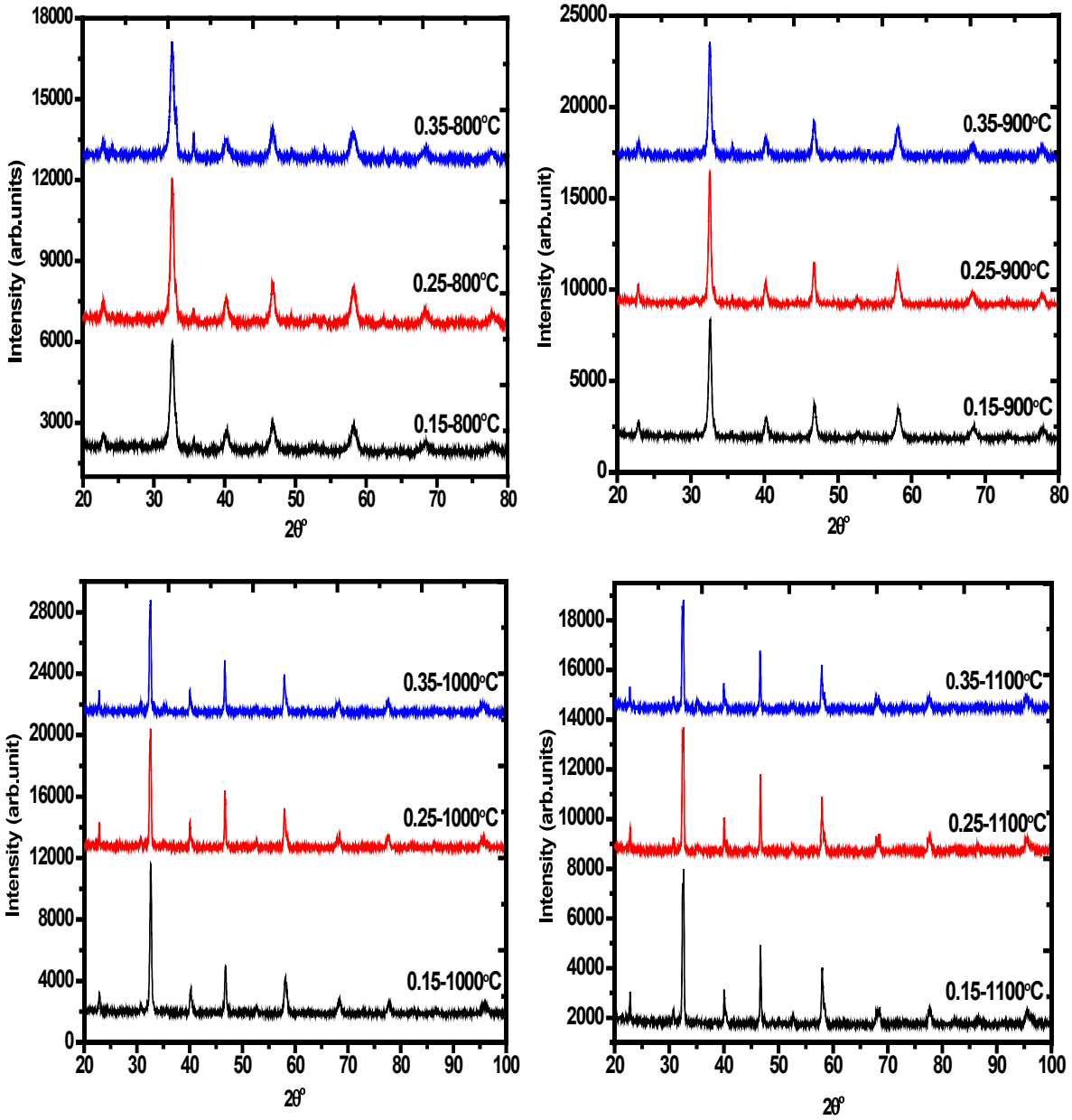

Fig. 4.4: The X-ray diffraction pattern of Fe doped LSMO manganite system.

The X-ray diffraction pattern of prepared samples were analyzed by Rietveld refinement using FullProf Software [30, 31] shown in Figs. 4.5 and 4.6. This program permits multiple phase refinements of each coexisting phase. The XRD spectra for different concentrations and calcination temperatures are divided in two figures. While Fig. 4.5 presents Fe doped samples for 800ºC and 900ºC, the Fig. 4.6 presents Fe doped samples for 1000ºC and 1100ºC respectively. The quality of the refinement is evaluated through several parameters such as the pattern R factor (R_f) and the goodness of fit indicator (χ^2). A good correspondence between experimental data and the fit is observed.

This shows that the Fe doped LSMO samples can be well indexed by rhombohedral lattice along with R-3c space group. The reflection peaks are indexed with standard JCPDS data which reveal rhombohedral perovskite crystal structure. The unfitted peaks were observed in the difference pattern at temperature 1100ºC. We have observed very less amount of secondary phase of Mn_3O_4 due to some experimental uncontrolled parameters [22]. In addition there exists a small peak around 31.08º which might be due to the $La(OH)_3$, as evident from earlier report [32]. This peak arises due to variation in atomic size of La and Sr. The value of FWHM is calculated to determine the crystallite size of nanoscale particles using Debye-Scherrer formula [33]. In Rietveld refinement the vertical lines are calculated Bragg's position of the reflections for rhombohedral compounds while the bottom lines showing the difference between the experimental and calculated XRD patterns. An unconstrained refinement of the data yields the LSMFO stoichiometries for the compounds with good values of R_f and χ^2 parameters listed in Table 4.1. The lattice, atomic and related parameters of the samples obtained by density functional theory are presented in Table 4.2. It is to be noted that the local spin density approximation (LSDA) calculations give a good agreement with experimentally obtained

structural and equilibrium parameters. The table shows that the lattice parameters increase with the increasing doping amount. This shows that the Fe substitution for Mn in ferromagnetic metallic compounds LSMFO does not change the crystal structure of system due to similar ionic radii of Fe^{3+} and Mn^{3+} ions [24, 34].

There appear some sharp peaks at (024), (404) and (128), indicating a good sign of phase formation [35]. Two peaks merge to give a single peak at (012) together with the rise in intensity of peak arising from plane (208) and (134). The unit cell parameters and volume show a systematic increase with increasing iron content. This can be attributed to the direct replacement of Mn^{3+} ion by identical sized Fe^{3+} which affects the Mn-O bond length and Mn-O-Mn angle in $La_{0.67}Sr_{0.33}Mn_{1-x}Fe_xO_3$ compounds [1, 23]. Average crystallite size (CS) is determined using Debye-Scherrer formula from XRD patterns as [36-38],

$$D = K\lambda/\beta\cos\theta \quad (2)$$

Where D is the average size of the particles, θ is the diffraction angle, λ is the wavelength and β is the full width at the half- maximum (FWHM) of XRD peak and K is the instrument constant which is 0.9.

The average crystallite size in nano $La_{0.67}Sr_{0.33}Mn_{1-x}Fe_xO_3$ (x=0.15, 0.25 and0.35) series increases with increasing Fe concentration. The formation of nanoscale LSMFO confirms the possibility of the synthesis of perovskite nanoparticles by planetary ball milling method. A reasonably good agreement is observed between the experimentally observed and density functional theory data for optimized structures.

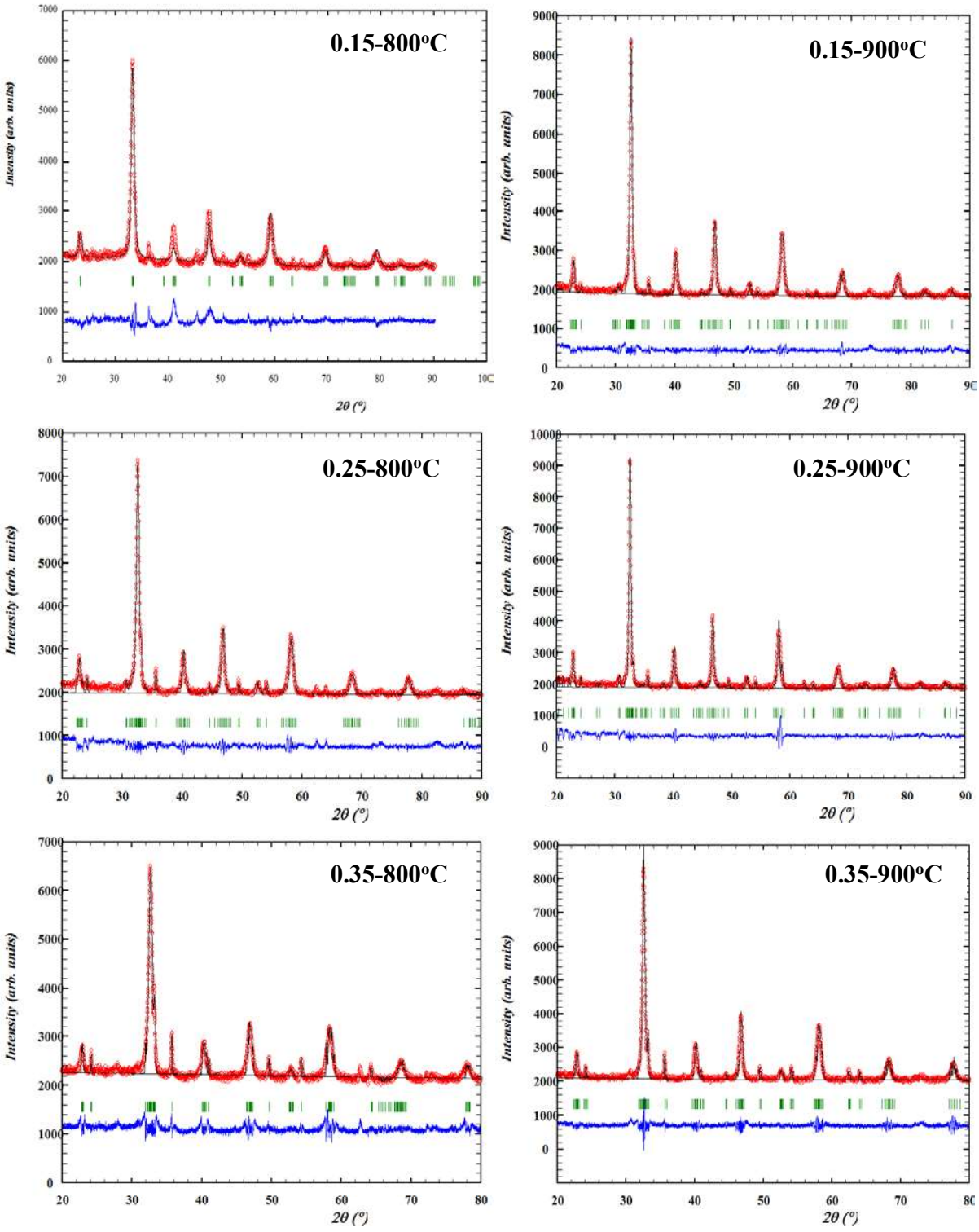

Fig: 4.5: Rietveld refinement analysis of Fe doped LSMO with different doping concentration (0.15 to 0.35) at various calcination temperatures (800°C and 900°C).

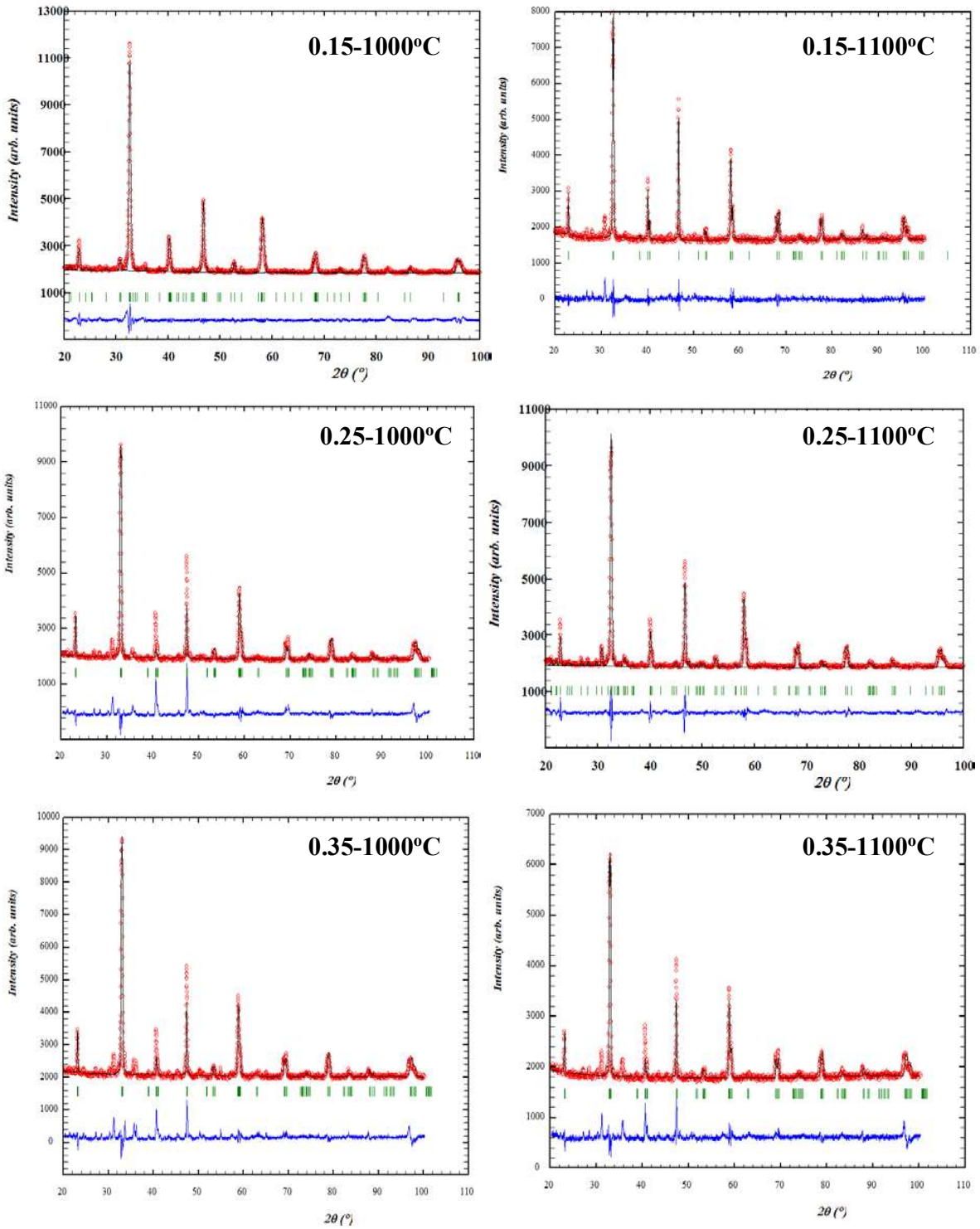

Fig. 4.6: Rietveld refinement analysis of Fe doped LSMO with different doping concentration (0.15 to 0.35) at various calcination temperatures (1000°C and 1100°C).

Table 4.1: Rietveld Refined structural parameters of Fe doped $LaSrMnO_3$ samples.

Sample	Lattice Parameter			Cell Vol. ($Å^3$)	Crystallite size D (nm)	Atomic position				Discrepancy Factor
	a (Å)	b(Å)	c(Å)				x	y	z	
x=0.15 (800°C)	5.4194	5.4194	13.17	334.99	21	La/Sr Mn/Fe O	0.000 0.000 0.458	0.000 0.000 0.000	0.250 0.000 0.250	R_p = 38.7 R_{wp} = 23.2 R_e = 17.6 χ^2 = 1.74 GOF= 1.31
x=0.25 (800°C)	5.4201	5.4201	13.186	335.49	24	La/Sr Mn/Fe O	0.000 0.000 0.547	0.000 0.000 0.000	0.250 0.000 0.250	R_p = 37.0 R_{wp} = 21.6 R_e = 15.0 χ^2 = 2.07 GOF= 1.44
x=0.35 (800°C)	5.5129	5.5129	13.59	357.88	27	La/Sr Mn/Fe O	0.000 0.000 0.535	0.000 0.000 0.000	0.250 0.000 0.250	R_p = 67.1 R_{wp} = 27.3 R_e = 16.1 χ^2 = 2.8 GOF= 1.69
x=0.15 (900°C)	5.4182	5.4182	13.188	335.31	19	La/Sr Mn/Fe O	0.000 0.000 0.448	0.000 0.000 0.000	0.250 0.000 0.250	R_p = 30.9 R_{wp} = 20.3 R_e = 13.7 χ^2 = 2.18 GOF= 1.48
x=0.25 (900°C)	5.4261	5.4261	13.186	339.65	25	La/Sr Mn/Fe O	0.000 0.000 0.466	0.000 0.000 0.000	0.250 0.000 0.250	R_p = 33.9 R_{wp} = 21.7 R_e = 13.3 χ^2 = 2.6 GOF= 1.63
x=0.35 (900°C)	5.538	5.538	13.473	357.94	34	La/Sr Mn/Fe O	0.000 0.000 0.510	0.000 0.000 0.000	0.250 0.000 0.250	R_p = 54.8 R_{wp} = 24.0 R_e = 13.3 χ^2 = 3.2 GOF= 1.80
x=0.15 (1000°C)	5.503	5.503	13.390	351.28	24	La/Sr Mn/Fe O	0.000 0.000 0.544	0.000 0.000 0.000	0.250 0.000 0.250	R_p = 33.7 R_{wp} = 18.0 R_e = 12.9 χ^2 = 1.94 GOF= 1.39
x=0.25 (1000°C)	5.438	5.438	13.20	338.18	35	La/Sr Mn/Fe O	0.000 0.000 0.478	0.000 0.000 0.000	0.250 0.000 0.250	R_p = 40.1 R_{wp} = 28.4 R_e = 12.7 χ^2 = 5.05 GOF= 2.23
x=0.35 (1000°C)	5.439	5.439	13.211	338.57	54	La/Sr Mn/Fe O	0.000 0.000 0.461	0.000 0.000 0.000	0.250 0.000 0.250	R_p = 38.1 R_{wp} = 23.4 R_e = 13.4 χ^2 = 3.08 GOF= 1.74
x=0.15 (1100°C)	5.509	5.509	13.375	351.59	32	La/Sr Mn/Fe O	0.000 0.000 0.453	0.000 0.000 0.000	0.250 0.000 0.250	R_p = 41.0 R_{wp} = 20.6 R_e = 15.7 χ^2 = 1.72 GOF= 1.31
x=0.25 (1100°C)	5.517	5.517	13.381	352.57	38	La/Sr Mn/Fe O	0.000 0.000 0.539	0.000 0.000 0.000	0.250 0.000 0.250	R_p = 56.2 R_{wp} = 23.0 R_e = 17.4 χ^2 = 1.73 GOF= 1.32
x=0.35 (1100°C)	5.519	5.519	13.393	353.37	60	La/Sr Mn/Fe O	0.000 0.000 0.545	0.000 0.000 0.000	0.250 0.000 0.250	R_p = 56.5 R_{wp} = 25.0 R_e = 19.3 χ^2 = 1.66 GOF= 1.29

Table 4.2: Optimized structural parameters of Fe doped LSMO using density functional theory.

Sample	Lattice Parameter, (Å)			Cell volume ($Å^3$)	Atomic position			
	a	b	c			x	y	Z
x=0.15 (800°C)	5.3851	5.3851	13.05	327.75	La/Sr	0.000	0.000	0.250
					Mn/Fe	0.000	0.000	0.000
					O	0.459	0.000	0.250
x=0.25 (800°C)	5.39006	5.39006	13.04	328.10	La/Sr	0.000	0.000	0.250
					Mn/Fe	0.000	0.000	0.000
					O	0.453	0.000	0.250
x=0.35 (800°C)	5.3552	5.3552	13.11	325.61	La/Sr	0.000	0.000	0.250
					Mn/Fe	0.000	0.000	0.000
					O	0.465	0.000	0.250
x=0.15 (900°C)	5.3949	5.3949	13.050	328.94	La/Sr	0.000	0.000	0.250
					Mn/Fe	0.000	0.000	0.000
					O	0.548	0.000	0.250
x=0.15 (1000°C)	5.384	5.384	13.046	327.51	La/Sr	0.000	0.000	0.250
					Mn/Fe	0.000	0.000	0.000
					O	0.456	0.000	0.250
x=0.15 (1100°C)	5.3914	5.3914	13.060	328.77	La/Sr	0.000	0.000	0.250
					Mn/Fe	0.000	0.000	0.000
					O	0.460	0.000	0.250

4.3.2 Morphological Properties

The surface morphological properties of the Fe doped $LaSrMnO_3$ ceramics prepared using ball milling method have been investigated using back scattered modefield emission scanning electron microscope (FE-SEM) using JEOL JSM-7600F model with operating voltage of 5 KV and 50.00 kx magnification. Figs.4.7and 4.8 presents the FE-SEM image of Fe doped LSMO. The FE-SEM images for different concentrations and calcination temperatures are divided in two figures. Fig. 4.7 presents Fe doped samples for 800ºC and 900ºC while Fig. 4.8 presents Fe doped samples for 1000ºC and 1100ºC. It is clear from FE-SEM micrograph that the particles possess spherical symmetry with non-uniformity. The observed grain size for synthesized samples is between 50-100 nm. The grain size increases with temperature. Obviously, the crystallite size calculated by XRD is several times smaller than the grain size obtained using FE-SEM. This difference may be because of the fact that grains are composed of several crystallites probably due to the internal stress or defects in the structure [38, 39]. All the tiny particles are in spherical shape. All compounds show very good grain connectivity with increasing Fe content. There is no detectable voids and porous in this samples. It is also clear from FE-SEM micrographs that the particles are highly agglomerated with irregular boundaries due to high homogeneity during synthesis at different doping concentration [1, 39]. Fig.4.9 shows transmission electron microscope (TEM) image of LSMO nanocrystalline samples comprising narrowly distributed particles. Since general features of FE-SEM images are almost similar for all samples, we have obtained a TEM image of one sample, x=0.15 at 800ºC. The average particle sizes estimated from the TEM micrograph considering the minimum large number of particles was found to be in the range 26 nm for x =0.15-800ºC.

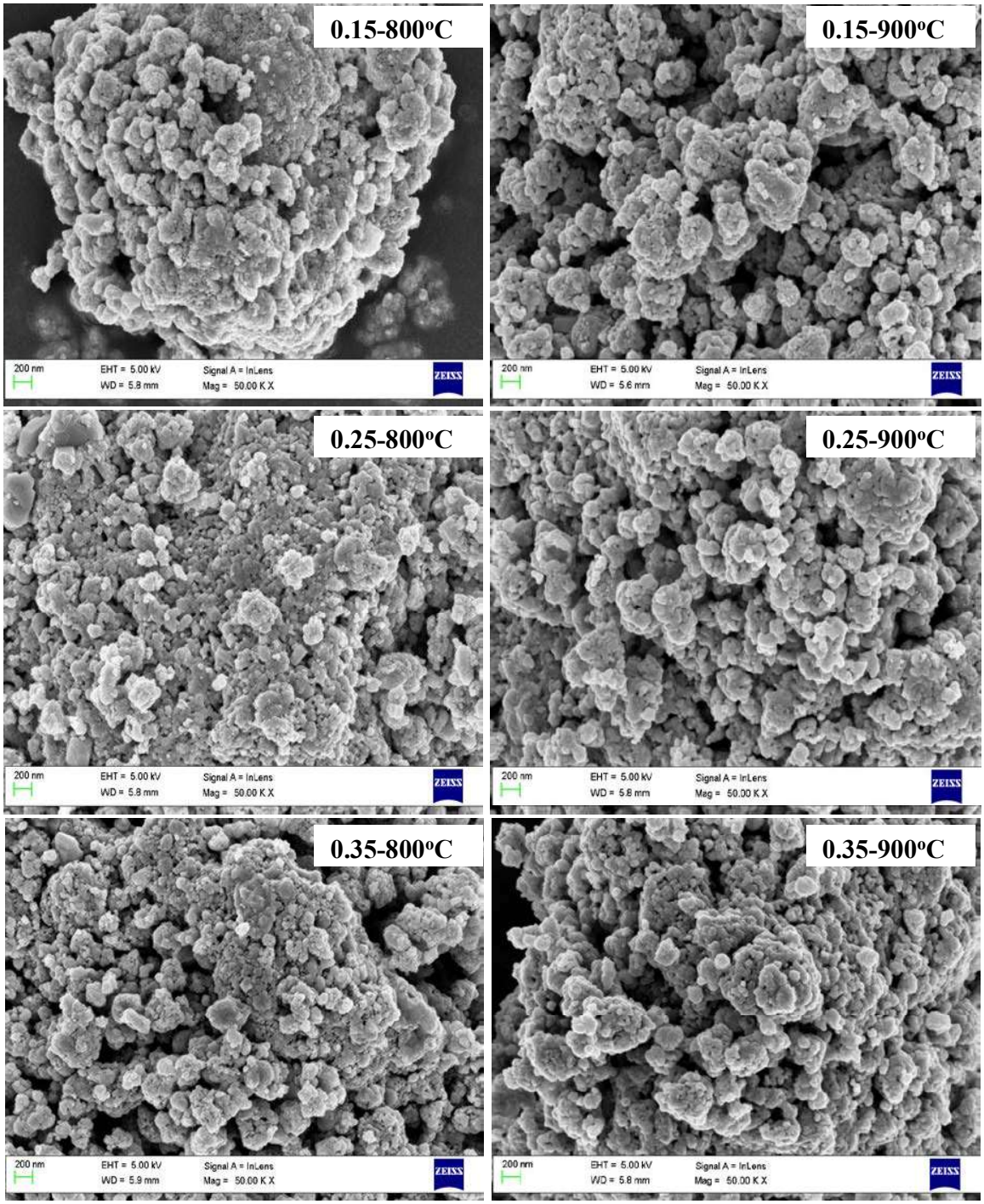

Fig. 4.7: FE-SEM micrograph of the Fe doped LSMO samples prepared at different calcination temperatures. The inset of figures displays concentration of Fe and calcination temperatures.

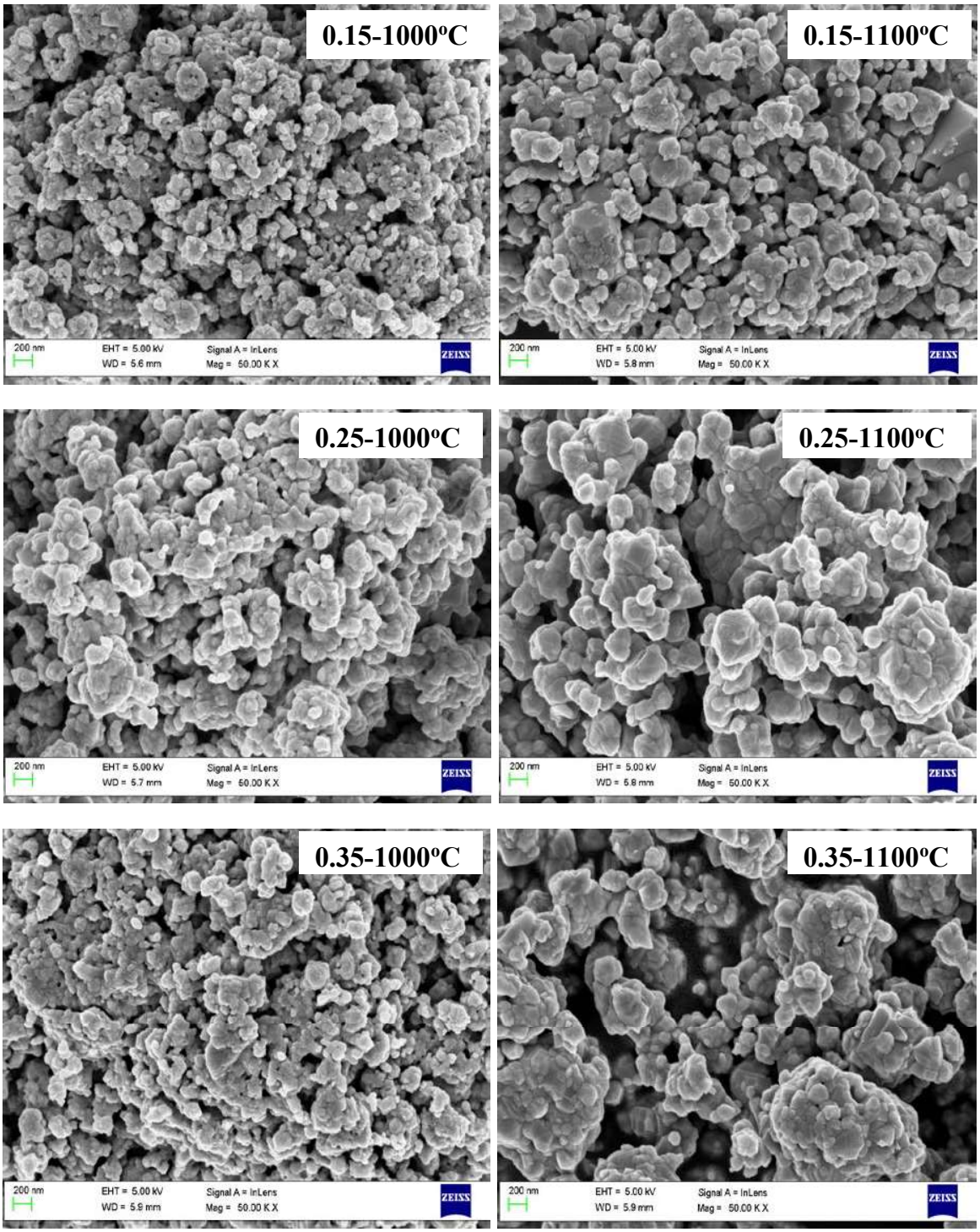

Fig. 4.8: FE-SEM micrograph of the Fe doped LSMO samples prepared at different calcination temperatures. The inset of figures displays concentration of Fe and calcination temperatures.

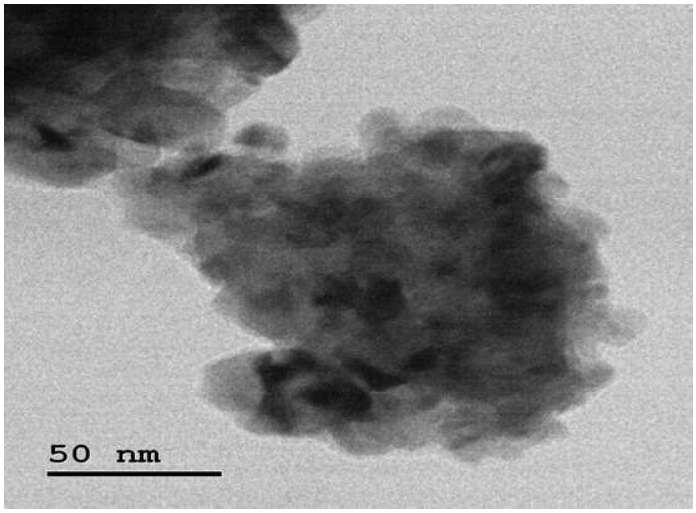

Fig. 4.9: TEM of Fe doped LSMO for x=0.15 at 800ºC calcination temperature.

4.3.3 Elemental Analysis (EDAX)

The quantitative elemental analysis of the ball milled prepared samples with different Fe concentration and calcination temperature is performed using energy dispersive analysis of X-ray (EDAX) spectra for quantitative elemental analysis of the composition of LSMFO prepared using ball milling. The peaks in the spectrum presented in Figs. 4.10 and 4.11 show the presence of La, Sr, Mn, Fe and O elements. The EDAX spectra for different concentration and calcination temperature are divided in two figures. While Fig. 4.10 presents Fe doped samples for 800ºC and 900ºC, the Fig. 4.11 presents Fe doped samples for 1000ºC and 1100ºC. EDAX spectrum of samples of all series is consistent with their elemental signals and stoichiometry. We do not observe any additional impurity peak which implies that the prepared samples are pure in nature. This is almost consistent with the nominal composition, suggesting that the obtained LSMFO samples are near stoichiometric [40]. The atomic weight compositions obtained from the EDAX spectra presented in Table 4.3 agree with the expected value which confirms the desired stoichiometry of the samples.

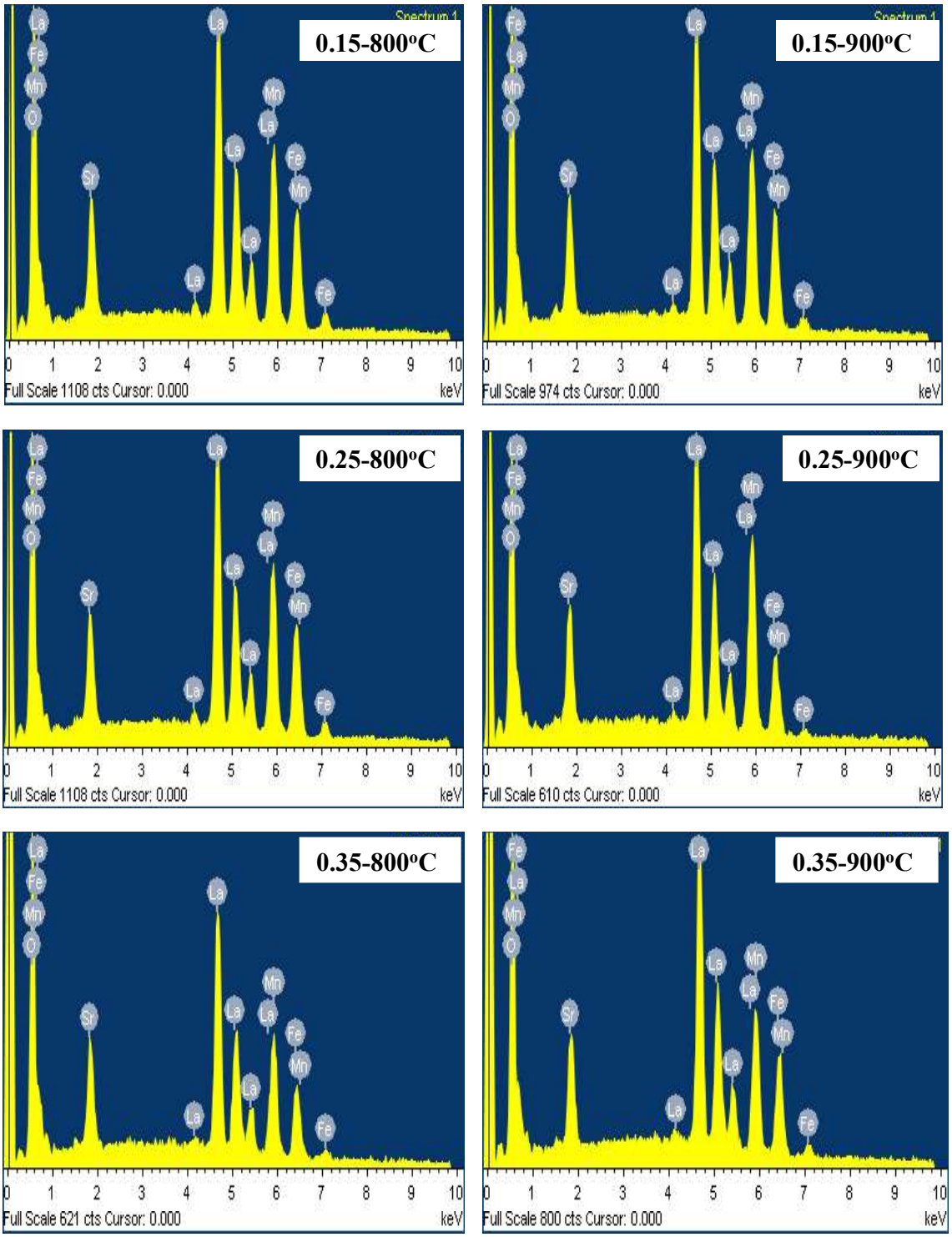

Fig. 4.10: EDAX spectra of LSMFO samples for different doping concentrations at various temperatures. The inset of figures displays concentration of Fe and calcination temperatures.

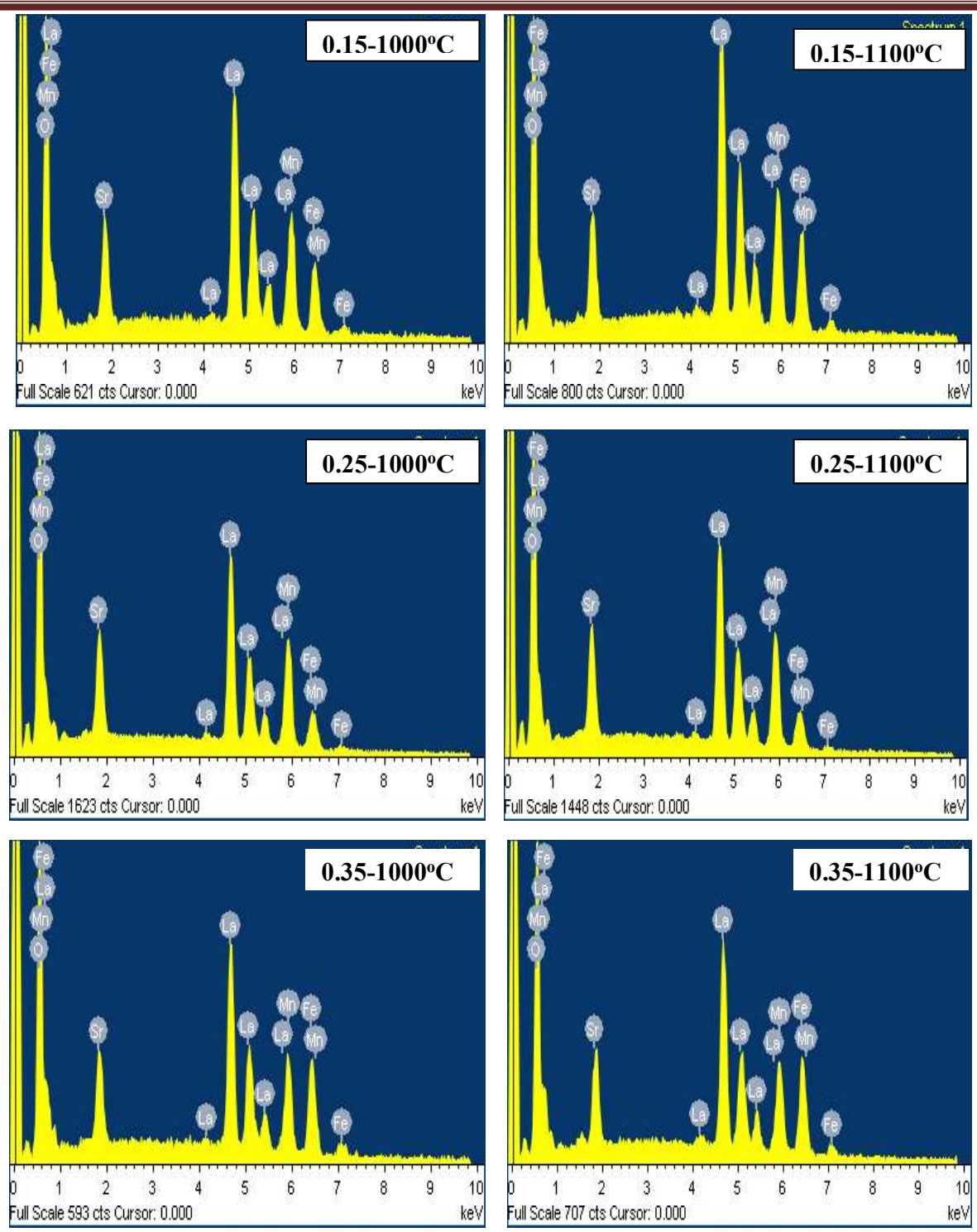

Fig. 4.11: EDAX spectra of Fe doped LSMOsamples for different doping concentrations at various temperatures. The inset of figures displays concentration of Fe and calcination temperatures.

Table 4.3: Atomic percentage of the EDAX pattern recorded of studied samples.

Sample	Atomic (%)					**Total**
	Element					
	La	Sr	Mn	Fe	O	
0.15 (800ºC)	10.98	3.97	11.03	3.73	70.29	**100**
0.25 (800ºC)	13.85	4.03	12.28	8.46	61.38	**100**
0.35 (800ºC)	13.27	3.61	9.66	12.74	60.73	**100**
0.15 (900ºC)	14.81	4.48	15.20	5.62	59.88	**100**
0.25 (900ºC)	13.49	3.88	11.71	8.24	62.69	**100**
0.35 (900ºC)	12.55	3.58	10.07	13.22	60.58	**100**
0.15 (1000ºC)	17.67	5.05	17.49	5.36	54.42	**100**
0.25 (1000ºC)	18.17	3.61	14.19	9.48	54.54	**100**
0.35 (1000ºC)	15.76	3.67	12.27	14.36	53.94	**100**
0.15 (1100ºC)	18.04	4.78	17.04	5.62	54.51	**100**
0.25 (1100ºC)	17.94	3.35	13.94	10.29	54.49	**100**
0.35 (1100ºC)	16.15	3.86	11.61	14.33	54.04	**100**

4.3.4 Vibrational Properties

Synthesis of the manganite nanoparticles with controlled properties is still a major challenge. Raman spectroscopy has appeared as a dominant nondestructive tool to characterize the nanoparticles and beenused to observe vibrational, rotational and other low-frequency modes in a system [16,17,20]. No phonon mode is Raman dynamic in cubic perovskite structure while

the orthorhombic or rhombohedral structure possessrise to Raman-dynamic phonon modes. It is accounted that the Raman dynamic A_{1g} and E_g modes are delicate to outside parameters [41].

In the Raman effect the electron excited in the scattering process decays to a different level than that where it started and is termed as inelastic scattering. Numerically, the energy difference between the initial and final vibrational levels, ω or Raman shift in wave numbers (cm^{-1}) can be expressed as; [42].

$$\nabla\omega = \left(\frac{1}{\lambda_0}\right) - \left(\frac{1}{\lambda_1}\right) \quad (3)$$

where $\nabla\omega$ is the Raman shift expressed in wavenumber, λ_0 is the excitation wavelength, and λ_1 is the Raman spectrum wavelength. In addition, the Raman spectroscopy is a powerful tool to investigate the driving force of the interplay of charge, spin, orbital and lattice degrees of freedom [43]. This makes possibility of getting information about the electron-phonon and spin phonon interactions.

Raman spectroscopy has been successively employed to investigate phonons and electronic excitations in various compounds of the manganite family [44-46]. Iliev et al. [44] have carried out a symmetry analysis of the important modes of the parent $LaMnO_3$ and structurally related perovskite compounds. The broadness of the modes over a large temperature region ruled out the effect of thermal broadening and is attributed to the phonon density of states (PDOS) related to strongly distorted oxygen sublattice. The Raman method is also quite useful for investigating the weak spin-reorientation transitions by selectively probing the magnons in the Mn^{3+} sublattices without considering the effects of paramagnetic moments of the rare earth ions.

The effect of Fe doping on the vibrational properties of Fe doped LSMO is studied by Raman Spectroscopy using JOBIN YVON HORIBA-HR800. The room temperature (300K) and low temperature (80K) Raman spectra of Fe doped LSMO are presented in Figs. 4.12 and 4.13 respectively.

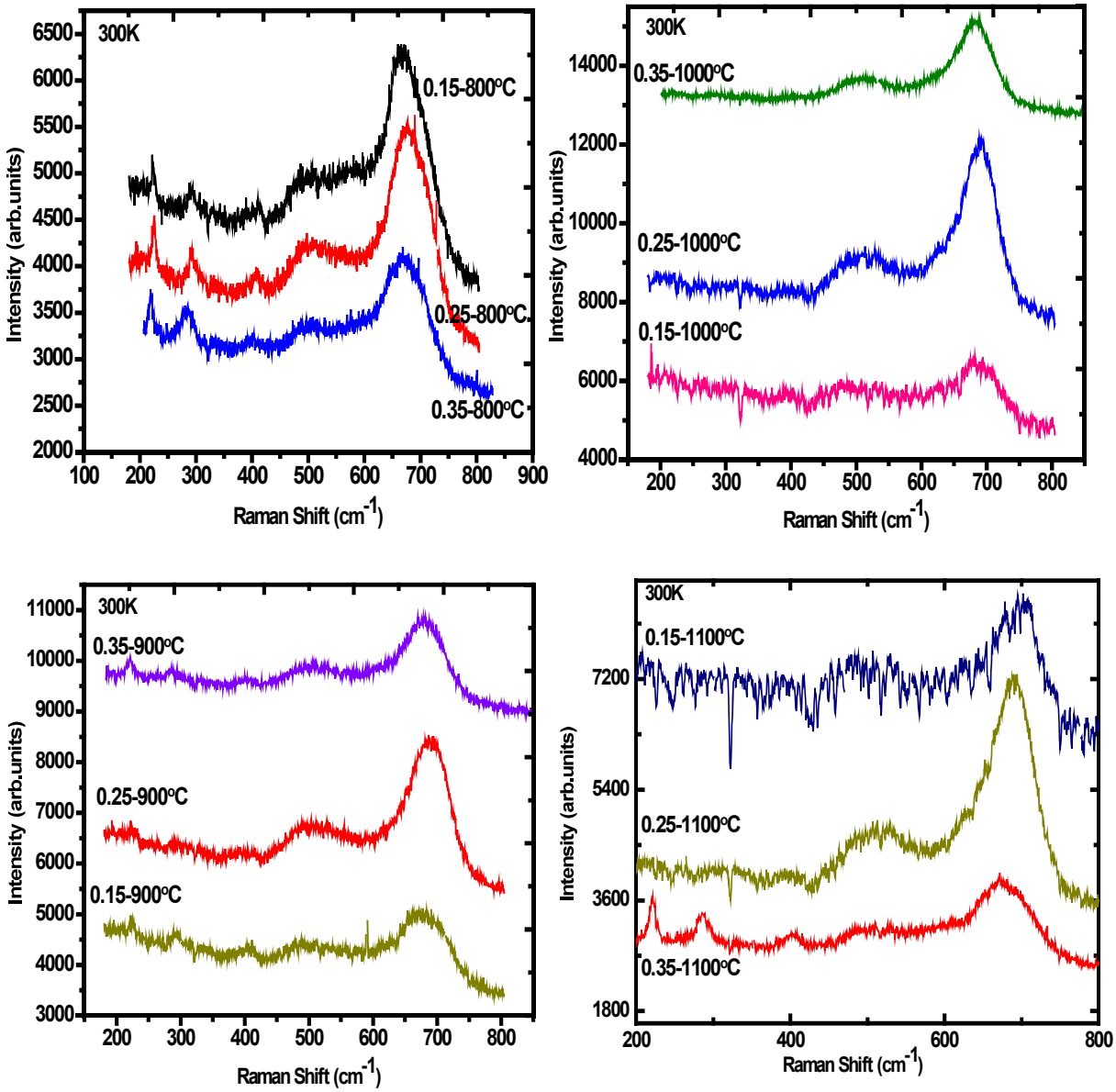

Fig. 4.12: Raman spectra of $La_{0.67}Sr_{0.33}Mn_{1-x}Fe_xO_3$ (x=0.15, 0.25 and 0.35) manganitesystem at room temperature (300K).

The present samples which are in rhombohedral structure (R-3c), with space group D^6_{3d}, Z=2 can be obtained from the simple cubic perovskite by the rotation of the adjacent MnO_6 octahedra in the opposite direction around the $[111]_c$ cubic direction [1, 44]. The theoretical and experimental descriptions of the Raman spectra have been briefed in Refs. [1]. There are five Raman (A_{1g} +$4E_g$) and eight infrared ($3A_{2u}$ + $5E_u$) active modes. Figs. 4.12 and 4.13 present the room and low (80K) temperature Raman spectra of Fe doped $La_{0.67}Sr_{0.3}MnO_3$compounds annealed at 800ºC to 1100ºC for 7 to 8 hours collected using 632.8 nm excitation wavelength in the frequency interval of 200-800 cm^{-1}. The A_{1g} mode only involves the vibrations of the oxygen ions in the C_2 sites while E_g modes arise both from oxygen and La (Sr) ions vibrations [1]. Based on Refs. [47, 48] low frequency peak around 220 cm^{-1} is assigned to A_{1g} symmetry while the peak around 414 cm^{-1} is assigned to E_g symmetry. There is a clear shift in both of these modes with varying doping content of Fe. The broader peak ≈ 670 cm^{-1} arising due to scattering induced by orthorhombic distortion shifts to higher wave number [1]. These are the characteristic modes of manganites arising from the Jahn-Teller distortions [49]. The broadening increases for both modes with Fe content indicating that the Jahn-Teller distortion increases with Fe concentration. Furthermore, the frequency shifts with doping results from the motion of oxygen cages and an effective octahedral rotation [50]. The compression which arises from stress due to the Fe doping at B site changes Mn-O bond length [1]. The obtained Raman mode frequency of LSMO sample annealed at 800ºC to 1100ºC with Fe doping of x=0.15, x= 0.25 and x=0.35 is presented in Table 4.4. The spectra have been discussed based on literature reports [44, 50]. Absence of one E_g mode might be due to the disorder produced in sample due to shift in position or vacancies of atoms around the oxygen atoms or change in Mn valency. The strong reduction of intensity and a further broadening of the phonon bands are observed on increasing doping. The Fe doping

concentration on various level changes the bond angle and bond length of Mn-O-Mn causing the octahedron of MnO_6 distorted [51].

Table 4.4: Raman mode position (cm^{-1}) of the prepared samples at room temperature (300 K) and low temperature at (80K).

Sample	300 K				80 K			
	A_{1g}	E_g	E_g	E_g	A_{1g}	E_g	E_g	E_g
0.15 (800°C)	224	292	410	670	228	293	414	665
0.25 (800°C)	225	293	408	675	228	295	413	678
0.35 (800°C)	221	286	409	675	226	292	414	675
0.15 (900°C)	224	294	411	674	228	296	416	676
0.25 (900°C)	221	289	415	688	228	301	415	696
0.35 (900°C)	221	294	404	678	227	294	411	683
0.15 (1000°C)	228	296	417	679	220	289	412	680
0.25 (1000°C)	219	290	418	693	214	284	411	694
0.35 (1000°C)	222	288	415	681	227	--	410	684
0.15 (1100°C)	229	308	410	690	215	286	417	691
0.25 (1100°C)	227	289	417	691	229	279	415	695
0.35 (1100°C)	221	285	408	677	228	--	414	685

Now let us focus on 80 K spectra. The broad bands are caused by distortion of the oxygen sublattice [1]. The E_g and A_{1g} modes which soften with the concentration harden with decreasing temperature. These are consistent with the Dubroka et al. [52] for other heavier ion doping at B-sites. The vibrational analysis which is also done using density functional theory (DFT) calculations show a substantial shift in A_{1g} and E_g modes with Fe doping. The E_g modes become broader with Fe doping.

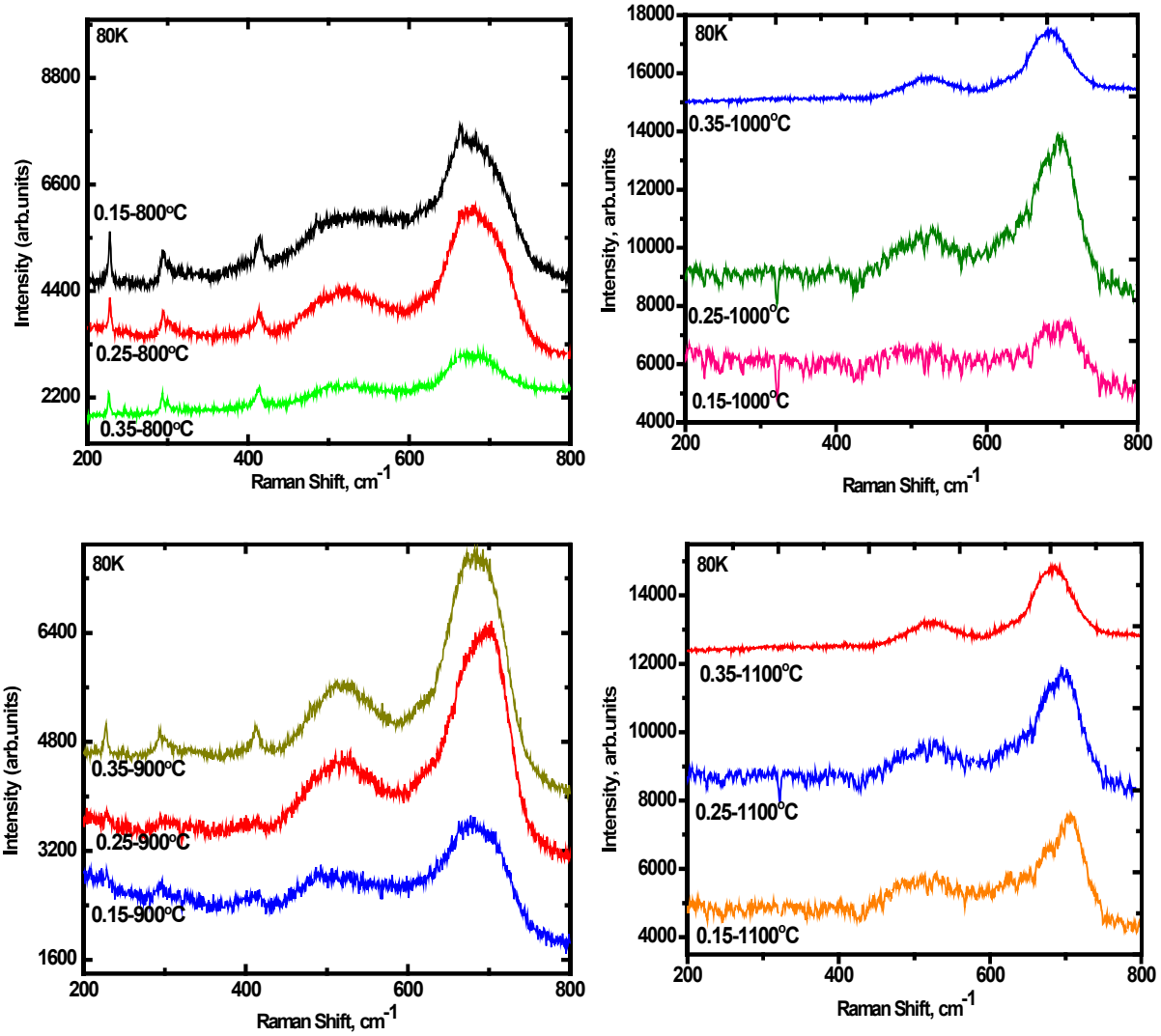

Fig. 4.13: Raman spectra of $La_{0.67}Sr_{0.33}Mn_{1-x}Fe_xO_3$ (x=0.15, 0.25 and 0.35) manganite system at low temperature (80K).

4.3.5 Magnetic Properties

The interest in CMR materials is not only due to their colossal magnetoresistance effect but also magnetic nature that this class of materials posses. The magnetic properties of the synthesized $La_{0.67}Sr_{0.33}Mn_{1-x}Fe_xO_3$ polycrystalline samples are investigated using SQUID PPMS Quantum design at UGC-DAE-CSR, Mumbai. We have studied the variation of magnetization as a function of temperature (M-T) and magnetic field (M-H) for some selected samples.

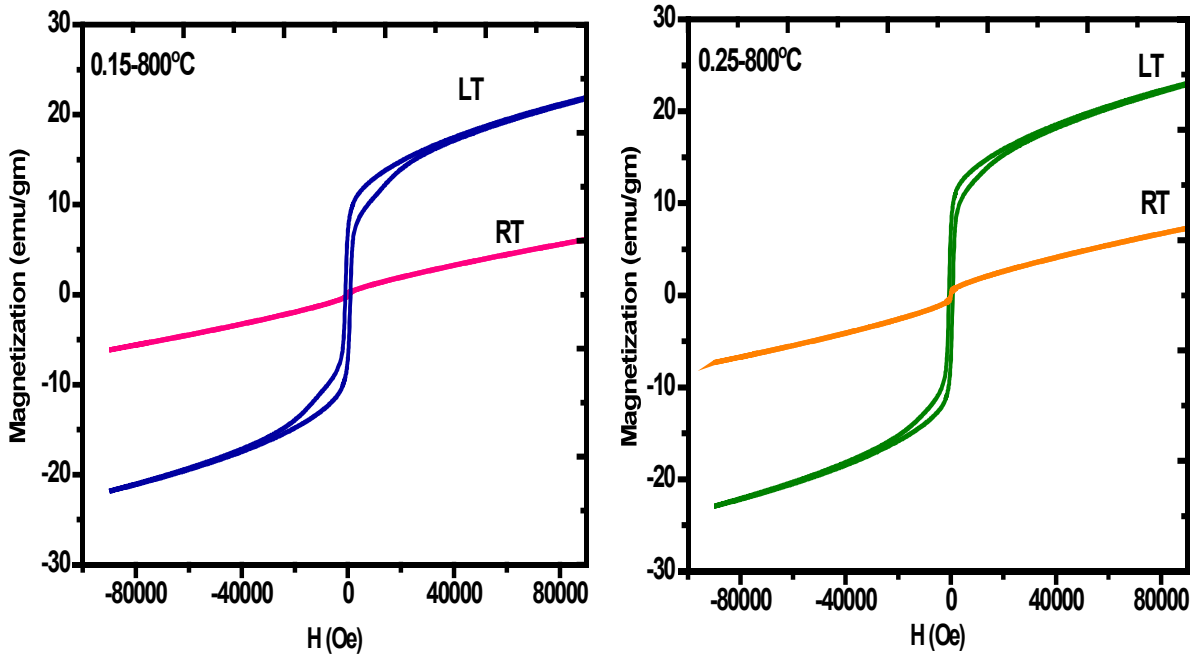

Fig. 4.14: Magnetic field dependence of magnetization (M-H curve) at LT (3K) and RT(300K) of LSMFO manganite materials.

LSMO particles at nanosize due to grain boundaries effects show significant differences in their physical properties with respect to the bulk material leading to important applications [15]. The magnetization vs temperature (M-T) and magnetization vs applied filed (M-H) curves respectively for samples; x=0.15, 0.25 are shown in Figs. 4.14 and 4.15. The magnetic properties

of the samples $La_{0.67}Sr_{0.33}Mn_{0.85}Fe_{0.15}O_3$ and $La_{0.67}Sr_{0.33}Mn_{0.85}Fe_{0.25}O_3$ are studied by vibrating sample magnetometer (VSM) at two temperatures 300 K and 3 K [53]. The saturation magnetization (M_s) observed at room temperature (RT) and low temperature (LT) respectively are 5.95 emu/gm and 21.83 emu/gm for x=0.15. However, same is observed as 7.23 and 22.93 emu/gm respectively at RT and LT for x=0.25. It is observed that the magnetization increases as the temperature increases. M-H curve clearly shows hysteresis loop. The magnetic anomaly in magnetic nanoparticles is observed at low temperature, which might be due to surface spin freezing effect of nano sized grains. Zhu et al. [54] noticed similar anomaly in field cooled magnetization of the same system.

The M–H curves clearly show irreversibility, which is consistent with the room-temperature ferromagnetism due to the double exchange between Mn^{3+} and Mn^{4+}. The Curie temperature for the samples x= 0.15 and 0.25 is T_C ~ 287 K and ~ 285 K respectively. The Curie temperature decreases as Fe concentration increases.

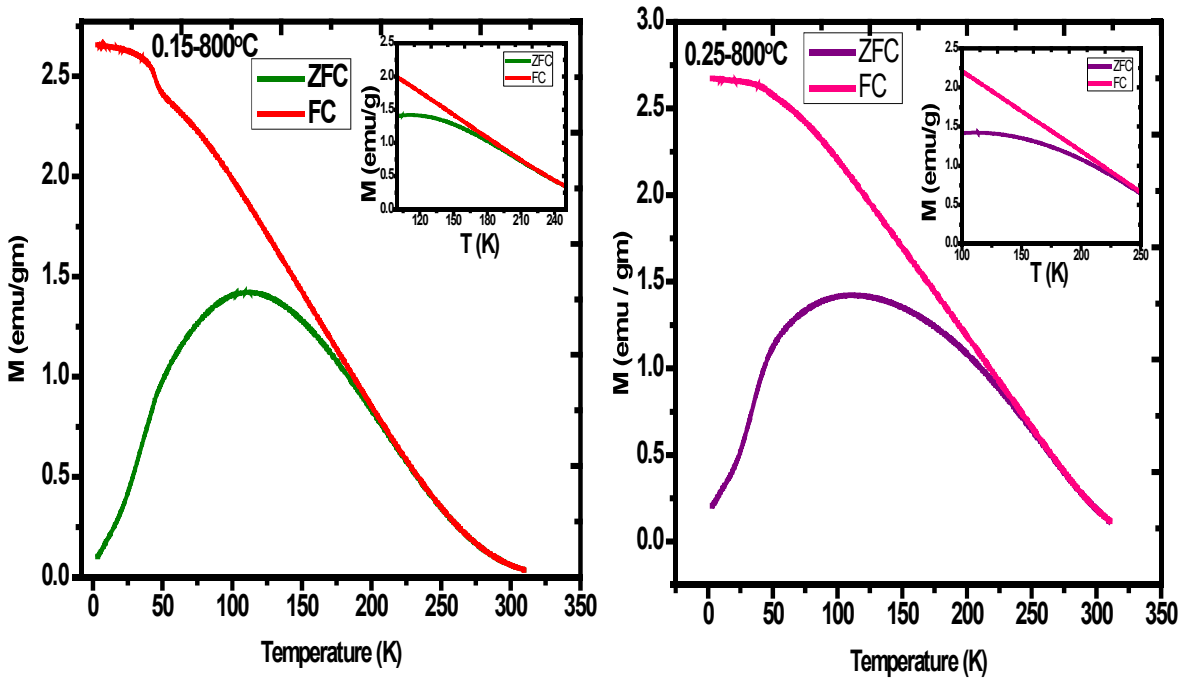

Fig. 4.15: Temperature dependences of ZFC and FC magnetization of x= 0.15, 0.25 at 100 Oe.

Fig. 4.15 shows the (ZFC) and (FC) magnetization curves for samples x= 0.15 and x = 0.25 at 800ºC in temperature range from 0 K to 350 K with 100 Oe applied magnetic field. It reveals that the ZFC and FC curves overlap on each other at temperature ~ 258 K. Overlapping of curve is a sign of superparamagnetism. It is clear that the sample x= 0.15 at 800ºC shows superparamagnetism (SPM). The magnetic irreversible temperature T_{irr} of the samples is 175 K, below which MFC increases. The blocking temperature T_B is 112 K, however the curve shows opposite behavior to that of MFC i.e. ZFC decreases. The decrease in ZFC is very sharp. The superimposition is due to dipolar interaction between the particles. Both samples show the ferromagnetic-paramagnetic transition. However, for the x=0.25 sample the ZFC and FC magnetization curves combine at temperature ~ 284 K which is a sign of superparamagnetism. The magnetic irreversible temperature, T_{irr} of the sample x=0.25 is 224 K.The blocking temperature T_B = 120 K for sample x=0.25 is higher than for x=0.15 for which T_B is 112 K. However, below the irreversibility temperature, the divergence between the two curves (ZFC and FC) is noticed for both samples. This type of behavior has been reported for other known magnetic systems such as spin glass and superparamagnet. The magnetic irreversible temperature increases with increase in concentration and observed that the same is dominated by the T_{irr} of the samples, synthesized using planetary ball milling method. The magnetic irreversible temperature illustrates high spin disorder in samples.

4.4 Density Functional Theory Calculations

The major aim of the present study is to perform the density functional theory (DFT) calculations for the prepared samples to understand their structural, electronic, magnetic and vibrational (Raman modes) properties. Therefore, a correlation between calculated and

experimentallyobtained results is necessary to find the process of formation of Fe doped LSMO by ball milling method and sol-gel methods. To have this understanding the obtained DFT results of these samples are discussed in light of present experimental data. While the optimization of structure with experimentally obtained structural parameters of all samples gives information about the formation, the spin polarized electronic calculations givesinformation about electronic as well as magnetic properties of samples. The latter is of great significant particularly in the absence of magnetic measurements for all samples. The comparison between calculated and experimental Raman modes will not only shed light on the formation of structure but also on the electron-phonon interaction leading to the understanding of Jahn-Teller distortion.

4.4.1 Computational Details

Ab-initio calculations in the present study for $La_{0.67}Sr_{0.33}Mn_{1-x}Fe_xO_3$(x=0.15, 0.25 and 0.35) have been performed within the local spin density approximation (LSDA) to the exchange correlation potential within the framework of density functional theory using the Vienna ab-initio simulation package (VASP) [1, 55]. We have used a unit cell of LSMFO to simulate the rhombohedral (R-3c) phase within the ferromagnetic (FM) ordering. Convergence tests on the energy cut off is 500 eV. The Brillouin zone sampling was performed according to Monkhorst-pack method [56] using the 10 × 10 × 10 grid and 12 × 12 × 12 **k**-points, whereas the density of states was calculated using the tetrahedron method [57] to generate the **k**-points within the irreducible wedge of the Brillouin zone. For structural optimization procedure each lattice parameter (a, b and c as well as the corresponding angles between them) and all internal structural degree of freedom (all atomic positions) have been fully relaxed. This ensures the proper optimization of the unit cell with zero pressure [58-60]. This complete geometrical optimization allows us to treat the structural path of the rhombohedral phase [61]. The starting

crystal parameters of the $La_{0.67}Sr_{0.33}Mn_{1-x}Fe_xO_3$ have been taken from our present XRD data of corresponding samples. Phonon calculations are performed using finite difference method. We have performed DFT calculations only for few selected samples due to heavy computation requirement.

4.4.2 Results and Discussion

The lattice and related structural parameters of all samples found using optimization of the structure obtained from Rietveld analysis of X-ray diffraction spectra are presented in Table 4.1. The optimization of a structure is to find minimum energy configuration. Fig. 4.17 presents the optimization curve of selected structures with respect to lattice parameters and energy cutoff values. Table 4.2 and 4.5 also consists the experimental parameters from present study. A good comparison is obtained between both.

Thermal stability of any system is one of the most important parameters that can be obtained by calculating the formation energy (enthalpy of formation) to know the stability of given system. In the present work, we have calculated formation energy of the systems using Hess's law that is a simplest process to calculate the enthalpy of formation. According to Hess's lawenthalpy of formation does not depend on intermediates in reaction; the total enthalpy change is equal to the sum of each individual reaction. If formation energy or enthalpy of formation (ΔH_F) is large and negative (exothermic reaction) then system will be formed i.e stable, while if it is small and negative then system are often stable butdecomposes easily and if it is positive (endothermic) then system is unstable.

Chemical reaction of given system is as follows:

$$0.335La_2O_3 + 0.33SrO + (1-x)MnO_2 + \frac{x}{2}Fe_2O_3 \rightarrow 0.67La_2O_3 + 0.33SrO + Mn(1-x)Fe_xO_3 \quad (4)$$

$$\Delta H_F = La_{0.67}Sr_{0.33}Mn_{1-x}Fe_xO_3 - [\text{Reactants}] \quad (5)$$

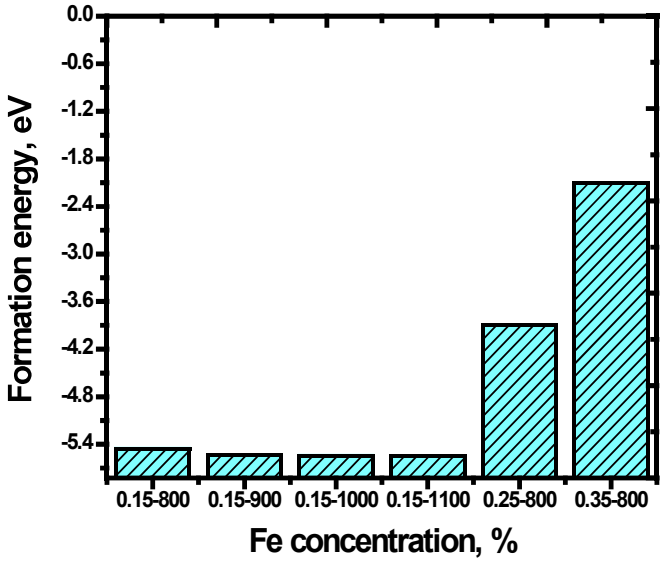

Fig. 4.16: Formation energy of x= 0.15 at 800ºC to 1100ºC and x=0.25 and 0.35 at 800ºC.

Fig. 4.16 shows the formation energy obtained by density functional theory. In this study, the first principle computations of the formation energy were carried out by using VASP simulation based on the DFT and plane-waves, with using the ultrasoft pseudopotentials. To estimate the relative stability of the inclusions, the formation energy for each inclusion was calculated. Formation energy is also a reflection of the ability of the compound to be formed. Equations (4) and (5) were adopted in the following calculations of formation energy for the compounds in our work.

Table 4.5 The calculated formation energy ΔH_F (eV) of Fe doped $LaSrMnO_3$.

Sample	Formation energy (eV)
x=0.15 at 800ºC	-5.454
x=0.25 at 800 ºC	-3.900
x=0.35 at 800 ºC	-2.110
x=0.15 at 900 ºC	-5.540
x=0.15 at 1000 ºC	-5.543
x=0.15 at 1100 ºC	-5.550

The calculated formation energy for few considered systems is presented in Table 4.5. By satisfying equation (4) and (5), we have plotted the formation energy diagram of Fe doped LSMO with different concentration at various calcination temperatures. The formation energy of -5.454 eV for x=0.15 at 800ºC, which is smallest value among the different kinds of inclusions, means that the Fe concentration of x=0.15 at 800ºC is most likely to form and followed by other doping concentrations. The formation energies of x=0.25 and 0.35 at 800ºC are -3.90 and -2.11 eV, much bigger than that of other inclusions (see Table 4.5). It also suggest that, x=0.15 at 800ºC is relatively more stable than two other x=0.25 and 0.35 respectively. In addition, x=0.15 at 1100ºC is thermodynamically more stable with respect to thoseformed at different calcination temperatures with same doping concentration. This result would indicate expected reductions in stability and electrochemical performance due to partial substitution of Mn with Fe. The higher thermodynamic stabilities of these x=0.15 at 800ºC compounds with increasing Fe contents might have a contribution to their improved electrochemical and thermal as seen by many researchers.

When the formation enthalpies of compounds are considered with respect to constituent oxides, the standard enthalpies of formation become less exothermic with increasing x. The main reason for the observed trend in enthalpy of formation from the oxides is the change in oxidation state of manganese in the constituent oxide. By increasing x (decreasing Mn content), the contribution of the exothermic oxidation of Mn^{3+} and Mn^{4+} to the overall enthalpy of formation decreases, resulting in enthalpies of formation which are less exothermic. Therefore, in cases where the oxidation states of the transition metals in reactants and products of formation reaction are dissimilar, the enthalpy of formation data from the constituent oxides may not reflect the real energetic trend. Instead, the enthalpy of formation from the elements is a better criterion for

assessing the relative thermodynamic stabilities in such systems. Fig. 4.17 shows the optimized lattice parameter and convergence energy curve using DFT.

The electronic structure calculations of the $La_{0.67}Sr_{0.33}Mn_{1-x}Fe_xO_3$ (LSMFO) samples were carried out by first principle calculation using density functional theory and compared with the obtained present and other available experimental data. The LSDA results give a strong ferromagnetic interaction without any sign of antiferrromagnetism for these systems. When compared with previous work [62], no significant changes are observed for the Mn-d states with increasing Fe content and only e_g states in the majority-spin channel contribute to the DOS at E_F. We have also calculated the total magnetic moment of the Mn atoms which are surrounded by different cationic environment [63]. We have not listed the contribution from La, Sr and O atoms to the total magnetic moment of the unit cell. The calculated magnetic moment of the unit cell is 16.52, 17.04 and 16.6 μ_B for x=0.15, 0.25 and 0.35 respectively, which are consistent with earlier report [64]. The enhancement of magnetic moments can be attributed to the change of complex interaction between Mn atoms and other atoms mainly the O atoms induced by octahedral rotation and deformation [65]. The average magnetic moment on the Mn atoms slightly increases from 2.49, 2.51 and 2.45 μ_B for x=0.15, 0.25 and 0.35 respectively [66]. To understand the effect of calcination temperature on the electronic band structure of Fe doping $La_{0.67}Sr_{0.33}MnO_3$, we have calculated electronic band structure of Fe doping with x= 0.15 for 800ºC, 900ºC, 1000ºC and 1100ºC and presented them in Fig. 4.18 (d-f).

To understand the origin of the ferromagnetism in the doped manganites it is necessary to understand their electronic structure. For this, first principle calculation based on density functional theory within the local spin density approximation (LSDA) implemented in VASP program were performed [67]. The electronic band structure is calculated at **Γ-M-A-L-**

Γsymmetric points in irreducible Brillouin zone and is shown in Fig. 4.18 with Fermi level at 0 eV. These LSMFO systems show metallic characteristic with conduction band minima (CBM) and valence band maxima (VBM) at **Γ** point of the Brillouin Zone for crystallographic phases. To understand more insight of the electronic properties, we have also computed the total density of states (TDOS) for LSMFO materials in rhombohedral crystallographic phases and shown in Fig. 4.18 which validates the electronic band structure. Thus, electronic states are the consequence of hybridization of respective cation and anion atomic orbitals as confirmed by their respective DOS spectra.

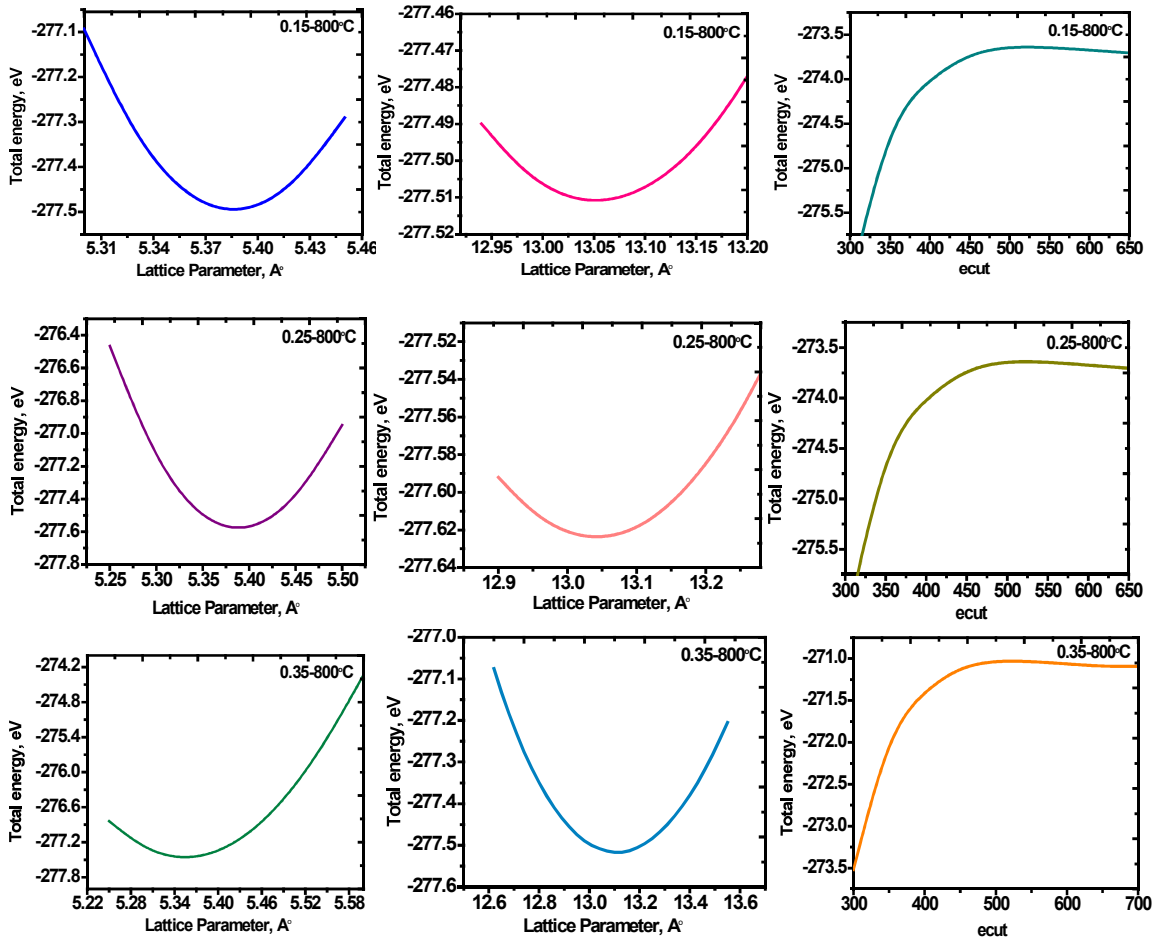

Fig. 4.17: Lattice parameter optimization and convergence of energy using DFT calculation.

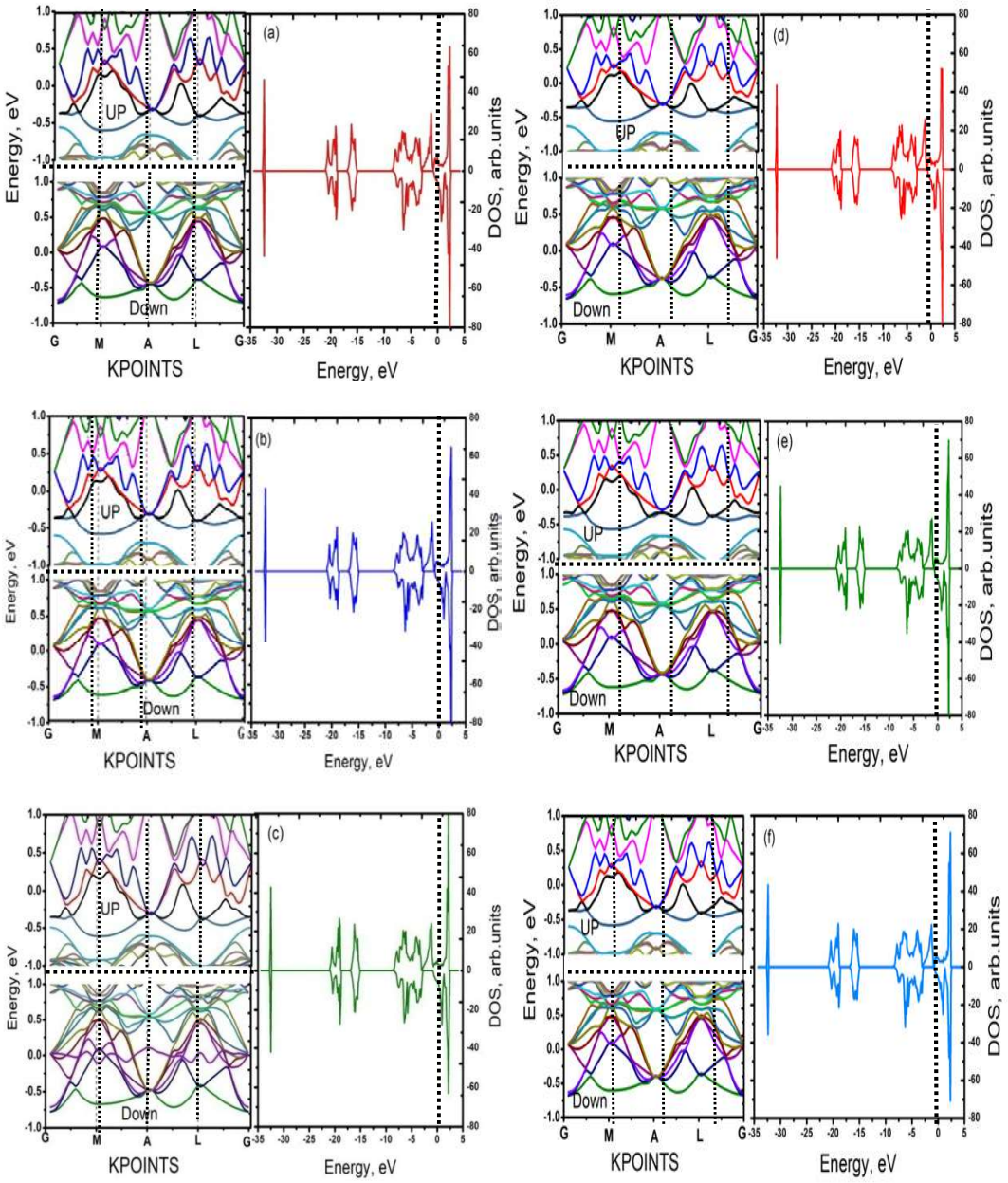

Fig. 4.18: Electronic bandstructure and total density states of Fe doped LSMO samples (a) 0.15-800ºC (b) 0.25-800ºC (c) 0.35-800ºC (d) 0.15-900ºC (e) 0.15-1000ºC (f) 0.15-1100ºC.

We have obtained the effective mass from the band structure calculations using the expression, $m^* = \frac{\square^2}{(2d)} \times m_e$. We observe that the effective mass of carriers $m^*/m_e$are 3.53, 3.98 and 4.95 for x=0.15, 0.25 and 0.35 respectively [50, 51]. The effective mass increases with

concentration. It is clarified that the deformation of $La_{0.67}Sr_{0.33}Mn_{1-x}Fe_xO_3$ polycrystalline has a significant influence on the effective mass due to the e_{2g} band flattening near the gamma point due to the Fe doping [51].

We have also performed the first principle calculation of Raman mode frequency of LSMO samples annealed at 800ºC with Fe doping of x=0.15, 0.25 and 0.35 and presented them in Table 4.6. There is a reasonably good agreement between both except the E_g mode for x=0.25. Our DFT calculated phonon frequencies show a substantial shift in both A_{1g} and E_g modes after Fe doping is consistent with the available other DFT [68], model [69] and experimental results [70]. The shift in frequency can be attributed to the distorted MnO_6 octahedra resulting from the change in bond angle and bond length. The Raman mode frequency of LSMFO sample calcined at 800ºC with Fe doping of x=0.15, 0.25 and 0.35 is presented in Table 4.6. There is a reasonably good agreement between experimental and theoretical both.

Table 4.6: Raman mode position (cm^{-1}) of the prepared samples at room temperature (300 K) using DFT.

Sample	300 K			
	A_{1g}	E_g	E_g	E_g
0.15 (800ºC)	226	298	409	686
0.25 (800ºC)	229	295	417	671
0.35 (800ºC)	221	299	410	675
0.15 (900ºC)	234	294	420	661
0.15 (1000ºC)	225	298	413	685
0.15 (1100ºC)	228	321	416	670

4.5 Conclusion

In summary, the Fe doped LSMO samples for various concentration of Fe at different temperatures are synthesized using planetary ball milling method to study the structural, surface morphology, elemental analysis, magnetic, electrical and vibrational properties. The density functional theory calculations are performed for samples with the help of their input structural data obtained for synthesized samples. The optimized structures are used to calculate the mentioned physical properties and are compared with obtained experimental data. The DFT calculationsare also used to understand the formation of Fe doped LSMO at different concentrations and calcination temperatures. Formation energy of x=0.15 at 800ºC is -5.45 eV, which is smallest value compared to other different concentrations at same 800ºC calcined temperature. From the formation energy it is understood that the Fe concentration of x=0.15 at 800ºC of ball milling method is better for the form of LSMFO sample compared to sol-gel route. In addition, x=0.15 at 1100ºC is thermodynamically more stable with respect for other different calcination temperatures at same doping concentration. Below Curie temperature (T_C), materials behave like metallic behavior and at low temperature the metal–insulator transition is observed.

Structural studies were carried out using XRD measurements confirm the crystallinity of the samples. The XRD spectra are good fitted with FullProf using Rietveld refinement. The lattice parameters and cell volume show increase with the increasing doping concentration (x). The morphological studies using FE-SEM show the agglomeration of the tiny particles with the spherical shape ranging between the 50-100 nm. A critical analysis of the micrographs show that the growth of grain size increases with increasing Fe concentration. The results of this elemental analysis match with stoichiometry of the compounds.

Raman spectroscopic measurements were carried out to study the variation in phonon frequency with Fe concentration and temperature. The peaks assigned in the Raman spectra are quite similar to the previous studies [52]. The Raman modes assign to various peaks is in good agreement with the rhombohedral structure. The temperature dependent Raman spectroscopic results show that the A_{1g} phonon mode which arises due to the rotation of MnO_6 octahedra is affected by the value of doping concentration. The experimentally observed feature of Raman spectra is consistent with the DFT calculated features. LSDA calculations reveal metallic behaviour without any intimation of antiferrromagnetism for these systems. The effective mass of carriers increases with increasing concentration of Fe from x=0.15 to 0.35.

The VSM studied using PPMS Quantum Design reveals ferromagnetic to paramagnetic phase transition in these systems. The saturation magnetization, blocking temperature, magnetic irreversible temperature and Curie temperature increase with increasing doping concentration. Superparamagnetic nature is observed for synthesized LSMO nano scale particles. The calculated formation energy follows the trend as -5.45, -3.90 and -2.11 eV respectively for x= 0.15, 0.25 and 0.35.

References

1. N. M. Astik, H. Soni, P. K. Jha and V. Sathe, Physica B: Condensed Matter 541, 103 (2018).
2. A. Urushi Y. Moritomo, A. Asamitsu and Y. Tokura, Phys. Rev. B 56, 12190 (1994).
3. A. P. Ramirez, J. Phys.: Condens. Matter. 9, 8171 (1997).
4. W. Prellier, Ph. Lecneur, C. Matrin and B. Raveau, J. Phys.: Condens. Matter. 13, R915 (2001).
5. F. Damay, A. Maigan, C. Martin and B. Raveau, J. Appl. Phys. 81, 1372 (1997).
6. D. Kumar and R. Singh Phys. Rev. B 56, 13666 (1997).
7. K. Ghosh, S. B. Ogle, R. Armes, R. L. Greene, T. Venkatesan, K. M. Gapchup, Ravi Bathe and S. I. Patil, Phys. Rev. B 59, 533 (1999).
8. C. Martin, A. Maignan, M. Herviev, C. Autret, B. Reveau and D. I. Khomskii, Phys. Rev. B 63, 174402 (2001).
9. J. M. D. Coey and M. Viret, Advances in Physics 48, 2, 167 (1999).
10. J. Topfer, J. Pierre Doumerc and J. Claude Grenier, J. Mater. Chem. 6, 1511 (1996).
11. J. A. M. van Roosmalen and E. H. P. Cordfunke, J. Solid State Chem. 110, 100 (1994).
12. R. Mahendiran, R. Mahesh, A.K. Raychaudhury and C.N.R. Rao, Pramana 44, L393 (1995).
13. A. Arulraj, R. Mahesh, G.N. Subbanna, R. Mahendiran, A.K. Raychaudhury and C.N.R. Rao, J. Solid State Chem. 127, 87 (1996).
14. C. Zener, Phys. Rev. 82, 403 (1951).
15. A. J. Milli, P.B. Littlewood and B. I. Shraiman, Phys. Rev. Lett. 74, 5144(1995).
16. A. Urushibara, Y. Moritomo, T. Arima, A. Asamitsu, G. Kido, Y. Tokura, Phys. Rev. B 51, 14102 (1995).
17. S. E. Lofland, S.M. Bhagat, C. Kown, S.D. Tiagi, Y.M. Mukovskii, S.G. Karabashev, A.M. Balbashov, J. Appl. Phys. 81, 548 (1997).
18. H. Chen and S. I. Beigi, Phys. Rev. B 86, 024433 (2012).
19. W. J. Lu, Y.Xie, G. B. Chen, F. L. Tang, Physica B: Condensed Matter 406, 1289 (2011).
20. M. Uehara, S. Mori, C. H. Chen and S.W. Cheong, Nature 399, 560 (1999).

21. V. Ravi, S.D. Kulkarni, V. Samuel, S.N. Kale, J. Mona, R. Rajgopal, A. Daundkar, P. S. Lahoti and R. S. Joshee, Ceramic International 33, 1129 (2007).
22. W. Cherif, M. Ellouze, A. F. Lehlooh, S. H. Mahmood, F. Elhalouani, Hyperfine Interact 211, 153 (2012).
23. N. Astik, P. K. Jha and A. Pratap, J. Electronic Mater. 47, 1937 (2018).
24. C. Hao, B. Zhao, G. Kuang and Y. Sun, Phys. Status Solidi B 248, 2921 (2011).
25. M. M. Jr. Xavier, F. A. O. Cabral, J. H. de Araujo, C. Chesman and T. Dumelow, Phys. Rev. B 63 012408 (2000)
26. Y. Sun, W. Tong, X. J. Xu, and Y. H. Zhang, Appl. Phys. Lett. 78, 643 (2001).
27. J. Gutierrez, A. Pen, J. M. Barandiaran, J. L. Pizarro, T. Hernandez, L. Lezama, M. Insausti and T. Rojo, Phys. Rev. B 61, 9028 (2000).
28. Y. Zhou, X. Zhu and S. Li, Ceramics International 43, 3679 (2017).
29. L. Joshi, S. Keshri, Measurement 44, 938 (2011).
30. J. Rodriguez Carvaje, Physica 192B, 55 (1993).
31. Y. Tokura, Phil. Trans. Roy. Soc. 356, 1469 (1998).
32. Y. Chen, Y. Wang, X. Liu, M. Lu, J. Cao and T. Wang, Nanoscale Research Letters 11, 538 (2016).
33. G. Venkataiah, V. Prasad and V. Reddy, J. Alloys and Compounds 429, 1 (2007).
34. W. X. Xianyu, B. H. Li, Z. N. Qian and H. M. Jin, J. Appl. Phys. 86, 5164 (1999).
35. I. P. Muthuselvam and R. N. Bhowmik, J. of Alloys and Compounds 511, 22 (2012).
36. P. Scherrer and G. Nachr, Gesell 2, 98 (1918).
37. M.A.M. Khan, M.W. Khan, M. Alhoshan, M.S. AlSalhi, A.S. Aldwayyan and M. Zulfequar, J. Alloys Compd. 503, 397 (2010).
38. Y. Tokura, Colossal Magnetoresistive Oxides, Advances in Condensed Matter Science 2, pp. 280 (2000).
39. K.P. Shinde, S. S. Pawar, N. G. Deshpande, J. M. Kim, Y. P. Lee and S. H. Pawara, Mater. Chemistry and Phys. 129, 180 (2011).
40. K. H. Ahn, X. W. Wu, K. Liu and C. L. Chien, Phys. Rev. B 54, 15299 (1996). Also see K. H. Ahn, X. W. Wu, K. Liu and C. L. Chien, J. Appl. Phys. 81, 5505 (1997).

41. P. K. Jha and M. Talati, A computational study of the phonon dynamics of some complex oxides, Computational Materials, Chap. 4, Ed. Wilhelm U. Oster, Nova Science Publisher, NY, pp. 177 (2009).
42. D. C. Harris and M. D. Bertolucci, Symmetry and spectroscopy: An introduction to vibrational and electronic spectroscopy, Oxford University Press, New York: pp. 388 (1978).
43. S. Mansouri, S. Jandl, A. Mukhin, V. Yu Ivanov and A. Balbashov, Scientific Reports 7, 13796 (2017).
44. M. N. Iliev, M. V. Abrashev, H. G. Lee, V. N. Popov, Y. Y. Sun, C. Thomsen, R. L. Meng and C. W. Chu, Phys. Rev. B 57, 2872 (1998).
45. S. Yoon, H. L. Liu, G. Schollerer, S. L. Cooper, P. D. Han, D. A. Payne, S. W. Cheong and Z Fisk, Phys. Rev. B 58, 2795 (1998).
46. M. M. Seikh, A. K. Sood and C. Narayana, Pramana J. of Phys. 64, 119 (2005).
47. B. C. Behera, A. V. Ravindra, P. Padhan and W. Prellier, Appl. Phys. Lett. 104, 092406 (2014).
48. L. Martin-Carron, A. de Andres, M. J. Martinez-Lope, M. T. Casais, and J. A. Alonso, Phys. Rev. B 66, 174303 (2002).
49. D. L. Rousseau, R. P. Bauman and S. P. S. Porto, Normal mode determination in crystals, J. Raman Spectroscopy, 10, 253 (1981).
50. A. E. Pantoja, H. J. Trodahl, A. Fainstein, R. G. Pregliasco, R. G. Buckely, G. Balakrishnan, M. R. Lees and D. Mck. Paul. Phys. Rev. B 63, 132406 (2001).
51. E. Granado, N. O. Moreno, A. Garcia, J. A. Sanjurjo, C. Rettori, I. Torriani, S. B. Oseroff, J. J. Neumeier, K. J. McClellan, S. W. Cheong and Y. Tokura, Phys. Rev. B 58, 11435 (1998).
52. A. Dubroka, J. Humlicek, M. V. Abrashev, Z. V. Popovic, F. Sapina and A. Cantarero, Phys. Rev. B 73, 224401 (2006).
53. A. V. Deshmukh, S. I. Patil, S. M. Bhagat, P. R. Sagdeo, R. J. Choudharyand D. M. Phase, J. Phys. D: Appl. Phys. 42, 185410 (2009).
54. T. Zhu, B.G. Shen, J.R. Sun, H.W. Zhao and W.S. Zhan, Appl. Phys. Lett. 78, 3863 (2001).

55. J. He, M.X. Chen, X. Q. Chen and C. Franchini, Phys. Rev. B 85, 195135 (2012).
56. H. J. Monkhorst and J. D. Pack, Phys. Rev. B 13, 5188 (1976).
57. O. Jepsen and O. K. Andersen, Solid State Commun. 9, 1763 (1971).
58. M. Talati and P. K. Jha, Phys. Rev. B 74, 134406 (2006).
59. B. C. Behera, A. V. Ravindra, P. Padhan and W. Prellier, Appl. Phys. Lett. 104, 092406 (2014).
60. L. Martin Carron, A. de Andres, M. J. Martinez Lope, M. T. Casais, and J. A. Alonso, Phys. Rev. B 66, 174303 (2002).
61. H. Jiangang, M. X. Chen, X. Q. Chen and C. Franchini, Phys. Rev. B 85, 195135 (2012).
62. J. E. Medvedeva, V. I. Anisimov, O. N. Mryasov and A. J. Freeman, J. Phys. Condens. Matter 14, 4533 (2002).
63. C. Ma, Z. Yang and S. Picozzi, J. Phys.: Condens. Matter 18, 7717 (2006).
64. J. Li, L. Sun, P. M Shenai, J. Wang, H. Zheng and Y. Zhao, J. of Alloys and Comp. 649, 973 (2015).
65. J. Li, Scientific Reports 6, 1 (2016).
66. P. Y. Vanina, A. A. Naberezhnov, V. I. Nizhankovskii and R. F. Mamin, Journal: Physics and Mathematics 2, 175 (2016).
67. W. X. Xianyu, B. H. Li, Z. N. Qian and H. M. Jin, J. Appl. Phys. 86, 5164 (1999).
68. M. Talati and P. K. Jha, Int. J. Mod. Phys. B 23, 4767 (2009).
69. M. V. Abrashev, A. P. Litvinchuk, M. N. Iliev, R. L. Meng, V. N. Popov, V. G. Ivanov, R. A. Chakalov and C. Thomsen, Phys. Rev. B 59, 4146 (1999).
70. P. T. Phong, S. J. Jang, B. T. Huy, Y. I. Lee and I. J. Lee, J. Mater. Sci. Mater. Electron 24, 2292 (2013).